A new interpolation method to measure delta evolution and sediment flux: Application to the late Holocene coastal plain of the Argens River in the western Mediterranean
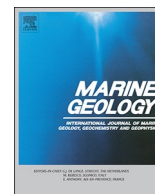
7 authors, including:

Some of the authors of this publication are also working on these related projects:

Project   RITMARE "First Phase" - Coastal Oceanography View project

Project   Climate change View project

A new interpolation method to measure delta evolution and sediment flux: Application to the late Holocene coastal plain of the Argens River in the western Mediterranean

Jean-Philippe Degeai[a],[*], Frédérique Bertoncello[b], Matteo Vacchi[c],[d], Laurent Augustin[e], Alain de Moya[e], Luigi Ardito[f], Benoît Devillers[a]

[a] ASM UMR5140, Université Montpellier 3, CNRS, Ministère de la Culture, 34199 Montpellier, France
[b] CEPAM UMR7264, Université Côte d'Azur, CNRS, 06357 Nice, France
[c] Dipartimento di Scienze della Terra, University of Pisa, Via Santa Maria 53, 56126 Pisa, Italy
[d] CIRSEC, Center for Climate Change Impact, University of Pisa, Via del Borghetto 80, 56124 Pisa, Italy
[e] DT INSU, C2FN, CNRS, 83507 La Seyne sur Mer, France
[f] BRGM, Centre scientifique et technique, 45060 Orléans, France

ARTICLE INFO

ABSTRACT

Rapid environmental changes along the Mediterranean coasts influenced the sedimentary dynamics, shoreline position and human settlements in deltaic areas over the last millennia. An innovative and multiproxy approach using geostatistical modelling was developed to estimate geomorphic evolution and sediment fluxes in deltaic areas, while palaeoecological conditions and environmental changes were assessed from geochemistry and cluster analyses of molluscan fauna. This method was applied to the coastal plain of the Argens River in southern France. Depositional environments of prodelta, delta front, river channel, floodplain, marsh and abandoned channel were identified from the study of facies associations. The late Holocene sediment flux in the Argens River bayhead delta ranged from $15,800 \pm 2300$ to $52,000 \pm 8500$ m$^3 \cdot$yr^{-1}. The highest rate of sediment deposition between 2500 and 2000 cal yr BP was associated with increased river flooding in southeastern France. A general decrease in subaqueous sediment flux over the past 2500 years was primarily controlled by a decrease in accommodation space and delta slope. From 500 to 0 cal yr BP, a sharp increase in subaerial sediment flux probably due to hydroclimatic change was contemporaneous with a period of high flood frequency during the Little Ice Age. A southward shift of the North Atlantic westerlies combined with either a negative phase of the East Atlantic/West Russian pattern or a negative phase of the East Atlantic pattern coupled to a northward migration of the intertropical convergence zone could have led to increased fluvial activity in the lower Argens valley during the late Holocene.

1. Introduction

In the western Mediterranean, the vulnerability of Holocene coastal landscape increased in response to rapid climate change characterized by pervasive millennial-scale variability as well as decadal- to centennial-scale abrupt transitions (Fletcher et al., 2013; Fletcher and Zielhofer, 2013; Melis et al., 2018). These rapid climate changes occurred during cooling events characterized by high storm activity and flood frequency, which led to an increased fluvial and coastal sediment supply (Dezileau et al., 2011, 2016; Sabatier et al., 2012; Fletcher and Zielhofer, 2013; Degeai et al., 2015, 2017). These episodes of intense storm activity and high flood frequency could have been caused by

changes in atmospheric circulation patterns such as the North Atlantic oscillation (NAO) or the intertropical convergence zone (ITCZ) (Benito et al., 2015a, 2015b; Goudeau et al., 2015; Dezileau et al., 2016; Sanchez-Lopez et al., 2016; Degeai et al., 2017).

For instance, a southward shift of the North Atlantic westerlies and storm tracks related to the negative phase of the NAO was associated with cooler and wetter climatic conditions in southwestern Europe during the Little Ice Age (Nieto-Moreno et al., 2011, 2013a, 2013b; Trouet et al., 2012; Wirth et al., 2013; Goudeau et al., 2014, 2015; Sanchez-Lopez et al., 2016). An increased river flooding and fluvial activity occurred at this time (Makclin et al., 2006; Benito et al., 2015a; Degeai et al., 2017), which led to higher inputs of terrigenous material

in the marine sediments of the western Mediterranean basin (Frigola et al., 2007; Nieto-Moreno et al., 2011, 2013a, 2013b; Goudeau et al., 2014, 2015; Jalali et al., 2016).

High fluvial sediment supply to coast and river mouths led to widespread coastal plains and an increased growth of bayhead deltas in incised-valley systems (Grove, 2001; Amorosi et al., 2009; Anthony et al., 2014). However, the quantitative impact of late Holocene climate change on the sedimentation rates and fluvial activity of western Mediterranean deltas is poorly known, although these coastal areas are important to estimate sediment transport and flux from continent to ocean, or to assess the balance between onshore erosion and offshore deposition.

The evolution of deltas developed in western Mediterranean incised-valley systems was generally characterized by facies associations showing a succession of marine, lagoonal or fluvial conditions over the past millennia (Amorosi et al., 2009, 2013a, 2013b, 2013c; Bertoncello et al., 2014; Anthony, 2015). The identification of depositional environment and the study of sedimentary processes and palaeogeographic changes in the western Mediterranean delta plains during the Holocene were generally based on multiproxy analyses of sedimentary sequences from cores or trenches (e.g. Giraudi et al., 2009; Bertoncello et al., 2014; Amorosi et al., 2016; Melis et al., 2018; Devillers et al., 2019; Ruiz-Pérez and Carmona, 2019). These methods are effective for coastal palaeoenvironmental reconstruction, but are often poorly suited to the geometric reconstruction of sedimentary units and the measurement of sediment volumes.

Geostatistics or numerical modelling was used to estimate palaeoelevation and sediment flux in coastal plains and incised-valley systems over the last millennia (e.g. Koster et al., 2017; Clement and Fuller, 2018). These interpolation methods are very useful in the case of limited age data and can provide important information on soil erosion, sediment flux, mass balance and geomorphic evolution in coastal areas.

In this paper, a new quantitative approach was developed to (1) calculate sediment flux associated with the progradation of bayhead deltas in incised-valley systems and (2) decipher the role of climate change and autogenic processes on delta growth. This new method was applied to the coastal plain of the Argens River in southeastern France, which is an area of particular interest for the study of atmospheric circulation patterns between northern and southern Europe. The depositional environment and sedimentary dynamics over the past 2500 years were studied using an integrated methodology based on cores and archaeological excavations, sedimentological analyses (geochemistry, magnetic susceptibility), malacology and radiocarbon chronology, then geomorphic change and sediment flux were estimated from geostatistics and elevation modelling. The variability of sediment flux was discussed in relation to late Holocene hydroclimate change and geomorphic setting.

2. Environmental setting

The Argens River drains a catchment of ca. 2800 km^2 located in southeastern France (Fig. 1A). This 114 km long river flows into the western Mediterranean between the Gulf of Lions and the Ligurian Sea along the southwestern Alps. This mountainous coastal area is bordered by a very narrow shelf (< 5 km) and a steep continental slope that stands above the floor of the Provençal Basin at depths > 2800 m. The source of the Argens River is at 268 m above sea level (Durozoy et al., 1970), giving an average slope of 2.35‰ for the modern streambed. Over the last 50 years (1970–2019), the hydrological regime at Roquebrune-sur-Argens (Fig. 1B) was characterized by maximum and minimum river discharge rates in winter (32.2 m$^3 \cdot$s^{-1}) and summer (5.8 m$^3 \cdot$s^{-1}), respectively, due to a Mediterranean rainfall regime (DREAL PACA data, www.hydro.eaufrance.fr).

The lower valley of the Argens River is bounded on the south by the late Proterozoic to early Carboniferous granitic and gneissic rocks of the Massif des Maures (Fig. 1B), and on the north by the Permian volcano-

sedimentary basin of the lower Argens valley (Toutin-Morin et al., 1994). At the end of the Last Glacial Maximum (LGM, ca. 20 cal kyr BP), sea level dropped > 100 m along the French Mediterranean coast (Lambeck and Bard, 2000), leading to an adjustment of the longitudinal profile of the river by regressive erosion (Bertoncello et al., 2014). Thus, the lower valley of the Argens River was deeply incised in Lower Pliocene marine sediments composed of blueish or grey marl, sand and gravel (Toutin-Morin et al., 1994). This incised-valley system was then buried by transgressive deposits during the post-LGM sea level rise (Dubar, 2004).

In the lower valley, the post-LGM deposits form a > 100 m thick sedimentary sequence composed of (1) fluvial sand and gravel at the bottom, (2) marine sand and clay intercalated with fluvial sand and gravel in the middle part, and (3) fluvial silt, sand and gravel at the top (Durozoy et al., 1970; Toutin-Morin et al., 1994; Dubar, 2004). The latter deposits were formed by delta progradation and fluvial aggradation, which led to the formation of a coastal plain over the past 4000 years (Dubar, 2004; Bertoncello et al., 2014). This coastal plain does not exceed 5 m in elevation over a distance of up to 5 km from the sea (Fig. 1B), giving a mean slope of 1‰.

Previous works studied the palaeogeographic and environmental changes in the Argens River coastal plain from the Neolithic to the Roman period and their impacts on human settlement (Dubar, 2004; Bertoncello et al., 2014). Over the past three centuries, historical maps or archives show a highly mobile coastal environment under the influence of the progradation of the Argens River along with the Garonne, Reyran and Villepey rivers (Fig. 1B) (Cohen, 1997; Bertoncello et al., 2008, 2014). In fact, these multiple channels formed a deltaic plain, hereafter called the Argens River delta system (ARDS).

The ARDS was classified as a bayhead delta that prograded into a protected bedrock embayment with low incident wave energy as a result of significant refraction, diffraction and nearshore dissipation (Anthony et al., 2014; Anthony, 2015). Bayhead deltas prograde in river-mouth setting along the inner part of wave-dominated estuaries (Dalrymple et al., 1992; Amorosi et al., 2005; Anthony et al., 2014), and become increasingly shaped by waves (Anthony, 2015). In the western Mediterranean, wave-dominated estuaries were filled with sediments during transgression then transformed into wave-dominated deltas during sea-level highstand (Amorosi and Milli, 2001; Milli et al., 2013). Confined or unconfined bayhead deltas are defined according to the geological and environmental setting: the former prograde into incised-valleys and their geometry is controlled by the morphology of the valley, while the latter prograde into open interdistributary bay and are a part of larger deltaic complexes (Simms and Rodriguez, 2015; Simms et al., 2018). The ARDS bayhead delta is confined in the Argens River valley west of Fréjus, and unconfined in the interdistributary bay between Saint-Raphaël and Saint-Aygulf (Fig. 1B).

During the Late Holocene, or the Meghalayan (i.e. the last 4200 years b2k), palaeoenvironmental and palaeoecological studies showed that the progradation of the ARDS occurred in a marine depositional environment that gradually transformed into a delta plain during the late phases of sedimentary filling of the lower valley (Allinne et al., 2006; Devillers and Bonnet, 2006; Bertoncello et al., 2014). Pollen data indicate that the first human impact on the landscape of the lower valley of the Argens River could have occurred around 7000 cal yr BP with indices of forest clearing and evidence of cereal cultivation during the late Neolithic period (Dubar et al., 2004; Bertoncello et al., 2014). After ca. 3000 cal yr BP, human activities led to high forest clearing and metal pollution in the sediments of the ARDS (Dubar et al., 2004; Bertoncello et al., 2014; Véron et al., 2018).

The past human occupation in the study area was more intense during the Roman period, especially from the creation of the Roman colony of *Forum Iulii* (Fréjus) (Fig. 1B) in the late first century BCE (Gascou, 1982; Gascou and Janon, 1985). The Roman harbour of *Forum Iulii* is now > 1 km inland from the sea owing to the progradation of the ARDS during the last two thousand years (Excoffon et al., 2006, 2010;
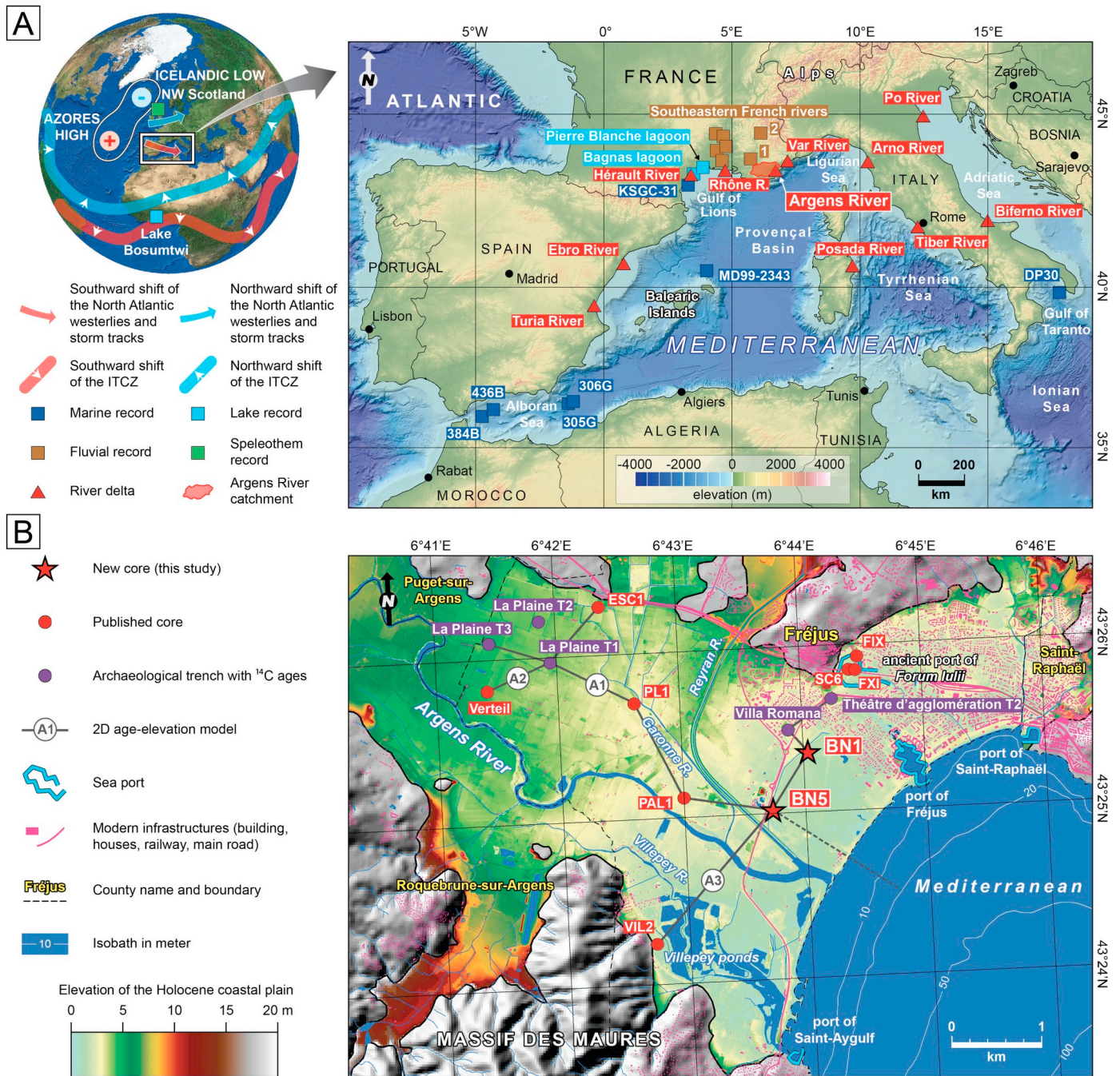
Fig. 1. Location of the Argens River in the northwestern Mediterranean (A) and topographic and geological setting of the Argens River delta system (B). Coordinate system: WGS 1984 World Mercator (A) and RGF 1993 Lambert-93 (B). ITCZ: intertropical convergence zone. 1, 2: Durance River sites (Arnaud-Fassetta et al., 2010; Benito et al., 2015a). References of published cores and archaeological surveys: Dubar (2004) for Verteil, Allinne et al. (2006) for ESC1, Devillers and Bonnet (2006) for VIL2, Excoffon et al. (2006) and Devillers et al. (2007) for Théâtre d'agglomération T2, Excoffon et al. (2010) for Villa Romana, Bony et al. (2011) for FIX, FXI and SC6, Bertoncello et al. (2014) for PL1 and PAL1, Bertoncello et al. (2016) for La Plaine T1 and T3.

Gébara and Morhange, 2010; Bertoncello et al., 2011; Bony et al., 2011; Giaime et al., 2019).

3. Material and methods

3.1. Cores and trenches

A geological database was created from sedimentary cores and archaeological trenches (Fig. 1B). It is based on published cores with geochronological and palaeoenvironmental data as well as on two new cores (BN1 and BN5) located in the downstream part of the ARDS. The 12-m long BN1 core (43°25′22″N, 6°44′02″E, 1.65 m in elevation) was sampled with a stationary piston corer. The 18.5-m long BN5 core (43°25′02″N, 6°43′44″E, 1.67 m in elevation) was sampled with a stationary piston corer from 0 to 3 m depth, a solid tube sampler equipped with a hydraulic hammer from 3 to 7 m depth, and a rotary drill auger from 7 to 18.5 m depth. The sediments at 3–4 m depth in BN1 and at 3.4–4 and 5.63–6.75 m depth in BN5 were unsampled due to creeping and difficulty in coring layers with very coarse particles.

Table 1
Radiocarbon dates from the Argens River delta system. Elevation in reference to LiDAR data (Litto3D, IGN/SHOM). LPT1: La Plaine T1, LPT3: La Plaine T3, TAT2: Théâtre d'agglomération T2. *: age inversion.

Core or trench	Elevation (m)	Laboratory code	Material	^{14}C age (BP)	Reference	2-σ interval of calibrated age (cal yr BP)	Median probability of calibrated age (cal yr BP)
BN1	0.30	Poz-81546	Charcoal	375 ± 30	This study	504–318	442
BN1	−3.60	Poz-81547	Charcoal	2520 ± 30	This study	2744–2492	2595*
BN1	−5.60	Poz-81608	Charcoal	2215 ± 30	This study	2322–2151	2231*
BN1	−7.00	Poz-81548	Charcoal	3330 ± 35	This study	3678–3467	3565*
BN1	−8.60	Poz-81549	Charcoal	2085 ± 30	This study	2143–1990	2058
BN1	−10.10	Poz-81550	Charcoal	2480 ± 30	This study	2723–2385	2585
BN5	−7.86	Lyon-13936	Wood	2055 ± 30	This study	2118–1934	2023*
BN5	−9.98	Lyon-13937	Wood	1975 ± 30	This study	1993–1871	1925
BN5	−12.33	Lyon-13938	Wood	2175 ± 30	This study	2310–2072	2231
BN5	−13.67	Lyon-13939	Wood	2195 ± 30	This study	2313–2133	2237
ESC1	0.18	Poz-12168	Seed	680 ± 30	Allinne et al. (2006)	680–561	652
ESC1	−1.57	Poz-12167	Seed	2535 ± 30	Allinne et al. (2006)	2747–2495	2625
ESC1	−2.52	Poz-12166	Seed	3735 ± 35	Allinne et al. (2006)	4227–3980	4089*
ESC1	−4.82	Poz-9593	Charcoal	3535 ± 35	Allinne et al. (2006)	3904–3702	3816
LPT1	3.44	Poz-78590	Charcoal	155 ± 30	Bertoncello et al. (2016)	284–0	174
LPT1	3.14	Poz-78591	Charcoal	175 ± 30	Bertoncello et al. (2016)	293–0	180
LPT1	2.44	Poz-78589	Charcoal	1315 ± 30	Bertoncello et al. (2016)	1295–1183	1259
LPT3	3.05	Poz-78593	Charcoal	4125 ± 30	Bertoncello et al. (2016)	4817–4531	4667*
LPT3	2.45	Poz-80846	Charcoal	960 ± 50	Bertoncello et al. (2016)	960–764	859
PAL1	−0.74	Lyon-5430	Seed	1075 ± 35	Bertoncello et al. (2014)	1057–930	982
PAL1	−1.84	Lyon-5431	Seed	1285 ± 35	Bertoncello et al. (2014)	1294–1097	1232*
PAL1	−2.34	Lyon-5432	Seed	1285 ± 35	Bertoncello et al. (2014)	1294–1097	1232
PAL1	−8.84	Lyon-5061	Seed	2145 ± 30	Bertoncello et al. (2014)	2304–2009	2137
PAL1	−14.34	Lyon-5062	Seed	2210 ± 30	Bertoncello et al. (2014)	2320–2149	2232
PAL1	−17.34	Lyon-5433	Seed	2800 ± 40	Bertoncello et al. (2014)	2998–2791	2904
PL1	1.49	Lyon-4223	Charcoal	1540 ± 35	Bertoncello et al. (2014)	1525–1356	1448
PL1	−1.21	Lyon-4221	Seed	2515 ± 40	Bertoncello et al. (2014)	2746–2467	2593*
PL1	−1.76	Lyon-4228	Seed	2510 ± 30	Bertoncello et al. (2014)	2740–2490	2590*
PL1	−3.41	Lyon-4226	Charcoal	3120 ± 35	Bertoncello et al. (2014)	3442–3234	3340*
PL1	−3.56	Lyon-5434	Seed	2395 ± 35	Bertoncello et al. (2014)	2687–2345	2425
PL1	−4.31	Lyon-4225	Charcoal	2450 ± 30	Bertoncello et al. (2014)	2704–2361	2528
PL1	−6.76	Lyon-4224	Seed	2490 ± 40	Bertoncello et al. (2014)	2738–2381	2583
PL1	−7.51	Lyon-5435	Charcoal	4200 ± 45	Bertoncello et al. (2014)	4851–4584	4730*
PL1	−8.81	Lyon-4222	Charcoal	2820 ± 35	Bertoncello et al. (2014)	3057–2846	2924*
PL1	−10.06	Lyon-4219	Charcoal	2610 ± 40	Bertoncello et al. (2014)	2843–2540	2749
TAT2	−0.33	Poz-14372	Marine shell	2345 ± 30	Devillers et al. (2007)	2087–1888	1983
Verteil	−2.41	Ly 5889	Peat	3050 ± 75	Dubar et al. (2004)	3443–3008	3247
VIL2	−2.25	Poz-10916	Charcoal	915 ± 30	Devillers and Bonnet (2006)	920–762	848
VIL2	−2.90	Poz-10917	Charcoal	1340 ± 30	Devillers and Bonnet (2006)	1305–1185	1280
VIL2	−5.65	Poz-10918	Charcoal	2325 ± 30	Devillers and Bonnet (2006)	2426–2208	2345
VIL2	−7.75	Poz-10922	Marine shell	5190 ± 30	Devillers and Bonnet (2006)	5634–5478	5571

3.2. Molluscan analysis

A volume of sediment of ca. 1000 cm³ per sample was collected at an average interval of 50 cm along BN1 and BN5 for a malacological study. These samples were sieved using a 1 mm mesh (Sabatier et al., 2008, 2012; Dezileau et al., 2016). A total of 2314 mollusc shells were identified and counted under stereomicroscope, representing 85 species living in marine (44 species), brackish (7 species), freshwater (17 species) or terrestrial (17 species) environments. The mollusc species were assigned to ecological groups from previous work in the Argens River valley (Devillers and Bonnet, 2006) and from the World Register of Marine Species (www.marinespecies.org), the AnimalBase of the University of Göttingen (www.animalbase.uni-goettingen.de) and the INPN database of the Museum National d'Histoire Naturelle (inpn.mnhn.fr).

3.3. Geochemistry

Geochemical analyses of sediments may provide information about the degree of salinity in coastal or lacustrine depositional environment, with high (low) values of S, Cl and Sr typical of brackish (freshwater)

conditions (Lopez-Buendia et al., 1999; Chagué-Goff et al., 2002; Schofield et al., 2010; Moreno et al., 2012; Haenssler et al., 2013; Degeai et al., 2015, 2017). Moreover, the bulk of sulphur in coastal lakes can reflect the organic content of a sediment as a function of primary productivity in the water column (Striewski et al., 2009; Haenssler et al., 2013). High ratios of S/Cl may indicate organic-rich layers as S is high in organic-rich sediments (Croudace et al., 2006). Besides, an increase in Si, K and Rb is generally associated with riverine input in the western Mediterranean (Frigola et al., 2007; Martin-Puertas et al., 2010, 2011; Nieto-Moreno et al., 2011, 2013a; Rodrigo-Gamiz et al., 2011, 2014; Moreno et al., 2012; Martinez-Ruiz et al., 2015; Degeai et al., 2017). Elemental concentrations in coastal sediments from the western Mediterranean are usually normalized to Al to minimize matrix effects (Dezileau et al., 2011, 2016; Sabatier et al., 2012). Therefore, we have used the Cl/Al and Sr/Al ratios as paleosalinity indicators, the Si/Al, K/Al and Rb/Al ratios as proxy records of riverine input, and the S/Cl ratio as an indicator of organic matter content.

A total of 108 and 138 sediment samples from BN1 and BN5, respectively, were measured by energy-dispersive X-ray fluorescence (ED-XRF) spectrometry at an average sampling interval of ca. 10 cm with a

Delta Innov-X spectrometer equipped with a 4 W Au-tube. Each sample was dried then mechanically crushed and homogenized to a fine powder, which was placed in a crystal polystyrene tube of 22 mm length and inner diameter then covered with an ultrafine polyethylene film. The measurement of S, Cl, Rb and Sr was undertaken with the soil analytical mode, while Al, Si and K were measured with the mining analytical mode. The parameters of voltage, amperage and counting times were as follows: 10 kV, 200 μA and 10 s for Al, Si and K; 15 kV, 200 μA and 45 s for S and Cl; 40 kV, 100 μA and 30 s for Rb and Sr. The elemental concentrations were obtained using the Compton Normalization calibration method (EPA, 2007). The 2-σ measurement uncertainty is lower than ± 5% for Si, K, Rb and Sr, and around ± 10% for S and Cl.

3.4. Magnetic susceptibility

In deltaic environment, the magnetic susceptibility can reflect the terrigenous flux derived from fluvial processes (Delile et al., 2015). Higher values of magnetic susceptibility are generally driven by the presence of Fe-bearing minerals (e.g. biotite) in the sample (Dearing, 1999).

The mass-specific magnetic susceptibility (χ) of sediments from BN1 and BN5 was measured at an average sampling interval of ca. 10 cm with a Bartington MS2 susceptibilimeter and a MS2B probe. Each powder sample in the tubes used for geochemical analyses (i.e. 246 samples for BN1 and BN5) was weighed then measured twice with a time period of 12 s, an operating frequency of 4.65 kHz, an amplitude of applied magnetic field of 250 μT, and a resolution of 1×10^{-8} kg·m^{-3} (range 0.1). The relative standard deviation of both measurements was systematically lower than 3%.

3.5. Geochronology

The geochronological data are based on a compilation of available radiocarbon ages in the ARDS, including a set of 10 new Accelerator Mass Spectrometry (AMS) ^{14}C dates on wood and charcoal from BN1 and BN5 (Table 1). The new AMS ^{14}C ages were performed by the Centre de Datation par le RadioCarbone at Lyon and by the Poznan Radiocarbon Laboratory. The CALIB 7.10 program (Stuiver et al., 2019) was used to calibrate the new ^{14}C dates and to recalibrate the previously published ^{14}C dates. The radiocarbon ages of terrestrial material (seed, wood, charcoal, peat) were calibrated using the IntCal13 calibration curve (Reimer et al., 2013), while the radiocarbon ages of marine shell were calibrated using the MARINE13 calibration curve (Reimer et al., 2013) and a ΔR of −15 years (Siani et al., 2000). The 2-σ uncertainty interval and the median probability of calibrated ages are reported in Table 1.

3.6. Geostatistics

Three 2D age-elevation transects (A1–3, see location in Fig. 1B) and five maps of sediment thickness in the ARDS were computed for the last 2500 years using the ArcGIS 10 Geostatistical Analyst extension. The geochronological and sediment thickness data were interpolated using radial basis functions. The computation of rasters of sediment thickness with a spatial cell of 15 m in size for each 500-year interval over the past 2500 years was based on the isochrones of the 2D age-elevation models and on a null thickness assigned to the boundary of Holocene deposits. The models were limited to the last 2500 years because there are not enough ^{14}C dates without age reversals to make a robust data interpolation before 2500 cal yr BP (Table 1).

The palaeoelevation Z_n was then calculated at a 500-year interval from $n = 1$ (500 cal yr BP) to 5 (2500 cal yr BP) using the ArcGIS 10 raster calculator and Eq. (1). For spatial coordinates (x, y), Z_n was obtained by subtracting the relative sea level S_n at the time n (Table 2) and the cumulative sediment thickness T from the modern elevation Z_0,

Table 2
Nominal relative sea level (RSL) with minimum and maximum errors from Vacchi et al. (2016). The RSL prediction was computed using the open source code SELEN (Spada and Stocchi, 2007) that employs the ICE-5G (VM2) model from Peltier (2004).

Age (cal yr BP)	Minimum RSL (m)	Nominal RSL (m)	Maximum RSL (m)
0	0.00	0.00	0.00
500	− 0.14	− 0.07	0.06
1000	− 0.28	− 0.13	0.12
1500	− 0.43	− 0.20	0.19
2000	− 0.58	− 0.28	0.26
2500	− 0.78	− 0.38	0.32

which is deduced from LiDAR data available for the ARDS (Litto3D, IGN/SHOM, year 2015).

$$Z_n(x,y) = Z_0(x,y) - S_n - \sum_{i=1}^{n} T_i(x,y) \tag{1}$$

Error estimates for sediment thickness and palaeoelevation were calculated with an uncertainty of ± 100 years for the isochrones of the 2D age-elevation models. This 200-year interval was chosen because it closely matches the mean 2-σ uncertainty interval (225 years) of calibrated radiocarbon ages (Table 1).

4. Results

4.1. Lithology

Both BN1 and BN5 cores were divided into 4 stratigraphic units from bottom (unit 1) to top (unit 4) (Figs. 2, 3).

Unit 1 in BN1 (12–9 m depth) is characterized by alternating 10–20 cm thick layers of grey to greyish brown clay, silt and fine sand (Fig. 2). Moreover, particulate organic matter is abundantly present in the matrix of sediments deposited from 11.8 to 10.2 m depth. In BN5, unit 1 (18.5–11.4 m depth) is primarily composed of grey clay and silty clay alternating with grey clayey silty fine sand at ca. 16 and 14.1–13.4 m depth, with brownish grey sand at ca. 18.4, 17.5, 16.8 and 16.4 m depth, and with grey sand and gravel at 16.5 and 12.7–12 m depth (Fig. 3). The clay content decreases above 14.85 m depth.

Unit 2 in BN1 (9–4 m depth) is mainly composed of grey, greyish brown, brownish grey or brown sand interbedded with silt and sandy silt (Fig. 2). The upper part shows a coarsening-upward trend from silt to medium-coarse sand. Thin organic-rich layers can be observed at 8.7–8.6, 8.25–8, 6.3–6.1 and 5.3–5.2 m depth, while charcoals are present around 5.7 m depth. In BN5, unit 2 (11.4–6.75 m depth) exhibits a succession of grey sediments characterized by a general coarsening-upward trend showing fine sandy silt and silty fine sand overlaid with fine sand from 8.5 to 8.1 m depth then with clayey medium-coarse sand and rounded gravel from 8.1 to 7.3 m depth (Fig. 3). Particulate organic matter appears at ca. 11.3–11.2, 9.6–9.4 and 8.7–8.5 m depth. The top of unit 2 in BN5 is composed of organic-rich grey clay between 7.3 and 6.75 m depth with black peat from ca. 7 to 7.2 m depth. This layer is absent in BN1.

Unit 3 in BN1 (3–1.4 m depth) is represented by brown sand and clast-supported rounded gravel showing a general upward-fining trend with fine-medium sand overlying coarse sand and gravel (Fig. 2). In BN5, the coarse sand and clast-supported rounded gravel of unit 3 (5.63–4 and 3.4–2.9 m depth) exhibit a brownish grey or greyish brown colour in the lower part and a brown colour above 4.85 m depth (Fig. 3). The bottom of this unit is uncertain in BN5 given the coring gap from 6.75 to 5.63 m depth.

Unit 4 in BN1 (1.4–0 m depth) is composed of brown clay, silt and fine sand with many rootlets and of a 20 cm thick dark brown clay layer at the bottom (Fig. 2). In BN5, unit 4 (2.9–0 m depth) is mainly composed of brownish grey or greyish brown fine sand interbedded with
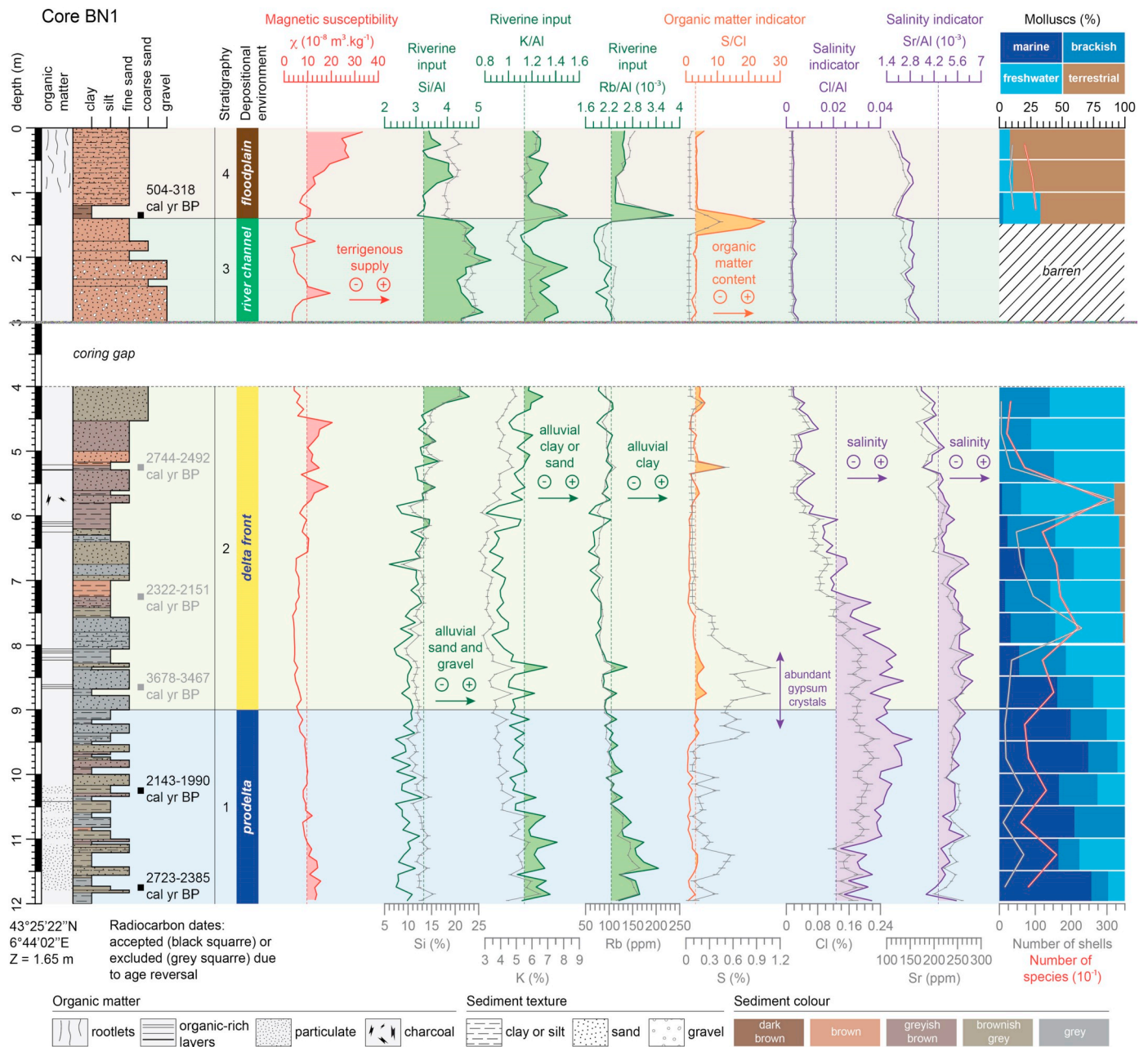
Fig. 2. Stratigraphy, magnetic susceptibility, geochemistry and malacofauna of core BN1 in the Argens River delta system. Vertical dashed lines correspond to the mean values of variables.

thin layers of clay and silty clay between 2.9 and 2.2 m depth, of greyish brown clay between 2.2 and 1.5 m depth, and of brown silt, clayey silt or fine sand between 1.5 and 0 m depth (Fig. 3). Small fragments of modern ceramics and a 15 cm thick layer of dark brown silt and matrix-supported angular or rounded gravel overlaid with a 4 cm thick layer of black organic silt appear in the upper 40 cm of BN5. Unit 4 in BN5 contains particulate organic matter, rootlets and charcoals.

Overall, bedding contacts are gradual apart from sand layers which are generally in sharp contact with clay or silt beds. Marine, brackish, freshwater gastropods and bivalves are present in units 1 and 2, while terrestrial gastropods are over-represented in unit 4. Unit 3 is barren of fossils.

4.2. Molluscan shells

The palaeoecological conditions prevailing in BN1 and BN5 were deduced from a multivariate cluster analysis of molluscan assemblages (Figs. 4, 5).

Unit 1 is characterized by a salinity-stressed marine environment with low to moderate brackish and freshwater influences. The dominant species of this ecosystem correspond to *Turbonilla lactea* in BN1 (41% on average) and to *Moerella donacina* in BN5 (19% on average). Subordinate marine species (1–10% on average) are represented by *Abra prismatica*, *Corbula gibba*, *Eulima bivittata*, *Macomangulus tenuis*, *Smaragdia viridis*, *Thracia pubescens*, *Trivia arctica* and *Trophonopsis muricata* in BN1, and by *A. prismatica*, *Acanthocardia* sp., *Antalis dentalis*,
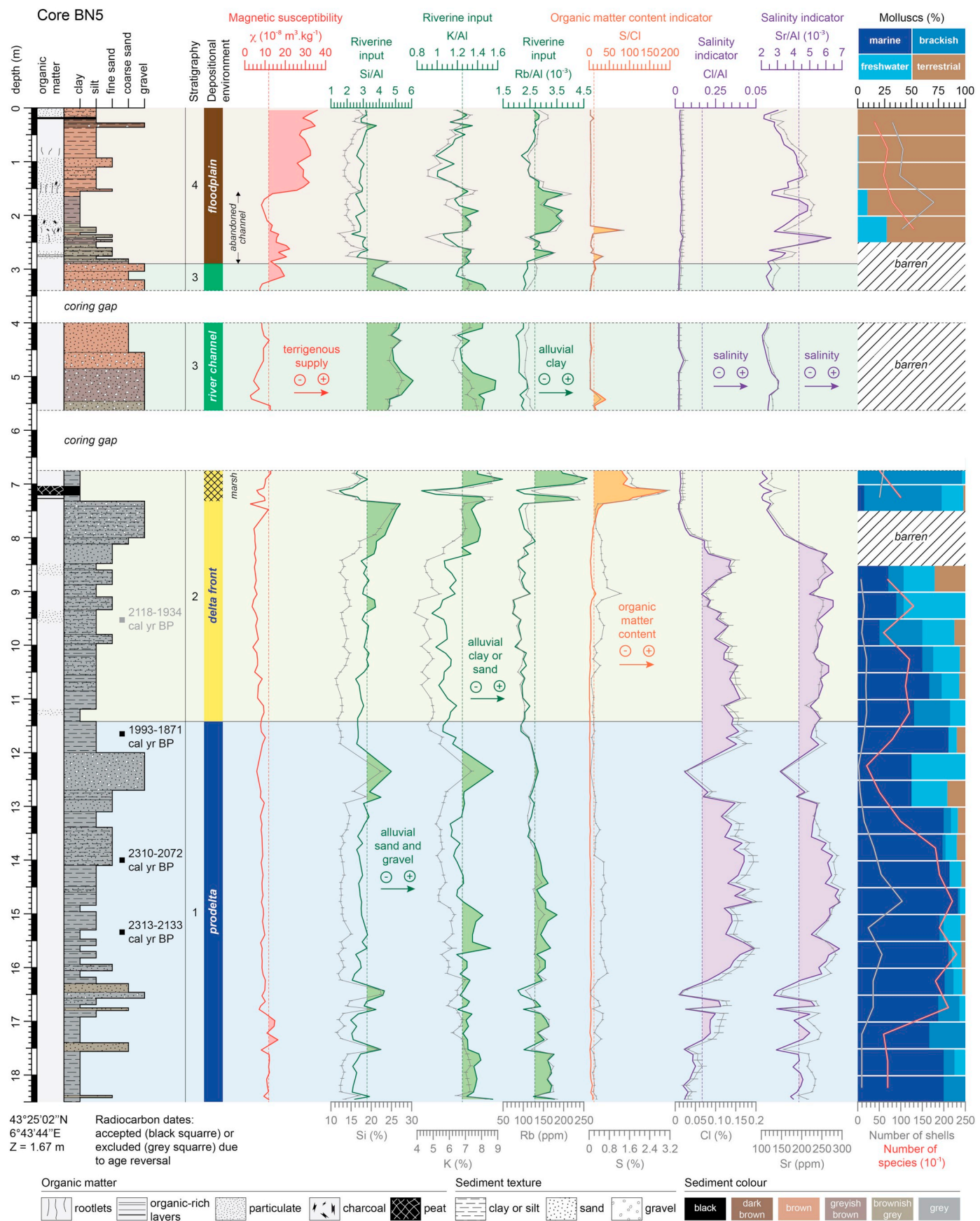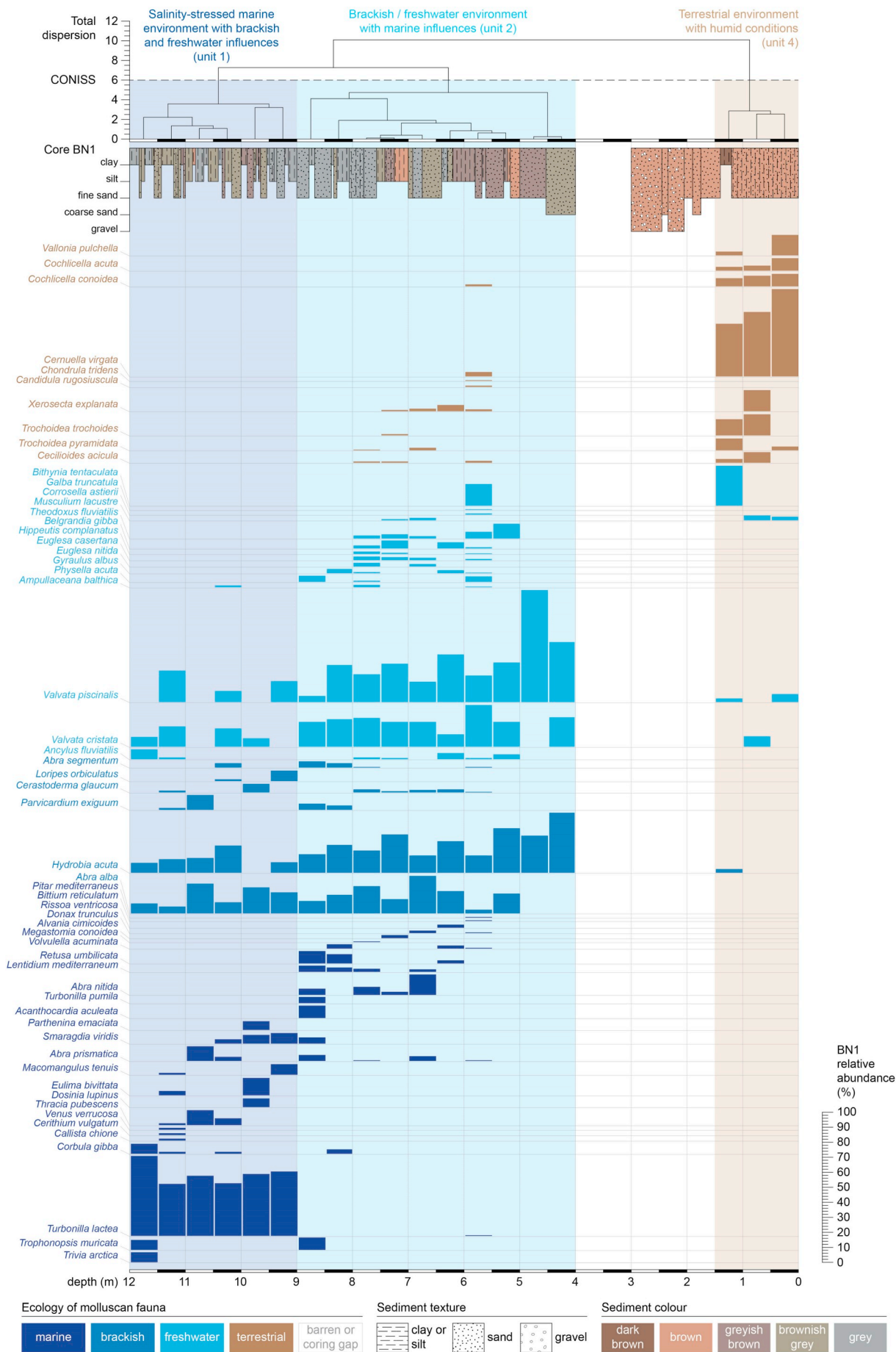
Fig. 3. Stratigraphy, magnetic susceptibility, geochemistry and malacofauna of core BN5 in the Argens River delta system. Vertical dashed lines correspond to the mean values of variables.

(caption on next page)

C. gibba, Gouldia minima, Lentidium mediterraneum, M. tenuis, Mathilda quadricarinata, Megastomia conoidea, Mimachlamys varia, Nucula nucleus, Saccella commutata and *Venus verrucosa* in BN5. A low to moderate mean abundance (1–12%) of molluscs such as *Abra alba, Cerastoderma glaucum, Hydrobia acuta, Loripes orbiculatus, Parvicardium exiguum, Ancylus fluviatilis, Bithynia tentaculata* and *Valvata* sp. suggests that the marine environment experienced brackish and freshwater conditions with fluvial discharges at BN1 and BN5.

Unit 2 is characterized by brackish and freshwater environmental conditions with marine influences (Figs. 4, 5). The molluscan assemblages are predominantly composed of *A. alba, C. glaucum, H. acuta* and *Valvata* sp. (> 10% on average in BN1 or BN5). Other subordinate brackish or freshwater species in BN1 or BN5 include *A. fluviatilis, Belgrandia gibba, B. tentaculata, Euglesa casertana* and *Theodoxus fluviatilis* (1–10% on average). The rare occurrence (< 1%) of terrestrial molluscs usually found in sandy dunes such as *Cernuella virgata, Cochlicella conoidea, Trochoidea trochoides* and *Xerosecta explanata* suggests reworking of coastal sediment, while a low to moderate mean abundance (1–12%) of *Abra nitida, A. prismatica, C. gibba, L. mediterraneum, Lucinella divaricata, M. donacina, N. nucleus, Retusa umbilicata,* and *T. lactea* in BN1 and/or BN5 highlights marine influences.

Unit 3 is barren of molluscan shells, whereas unit 4 is characterized by a terrestrial environment with low to moderate humid conditions (Figs. 4, 5). The most abundant land snails are represented in BN1 and BN5 by species living in dry habitats of coastal areas like sandy dunes or beaches: *C. virgata* (45 and 30% on average, respectively) and *C. conoidea* (7 and 43% on average, respectively). The most frequent subordinate terrestrial species (1–10% on average) correspond to gastropods living in dry vegetation or on sandy dunes in coastal areas (*Cochlicella acuta, Trochoidea pyramidata, T. trochoides, X. explanata*). Other uncommon land molluscs (< 6% on average) live in either humid habitats (*Cecilioides acicula, Oxychilus draparnaudi, Oxyloma elegans, Vallonia pulchella*) or open habitats with very variable humidity (*Vertigo pygmaea*). The main species of freshwater molluscs are *B. tentaculata, Galba truncatula, Musculium lacustre* and *Valvata* sp. (1–10% on average).

4.3. Geochemical data

Unit 1 generally exhibits high values of Cl/Al and Sr/Al, which reflect high levels of salinity (Figs. 2, 3). However, higher than average riverine inputs (K/Al and Rb/Al but not Si/Al) accompanied with lower values of Cl/Al and Sr/Al at the bottom of BN1 and BN5 could reveal fluvial influence in a marine depositional environment. The layers of brownish grey sand or grey sand and gravel in unit 1 of BN5 are associated with peaks of Si along with low levels of salinity (Fig. 3). These coarse sediments could reflect local and brief episodes of high-energy fluvial input. The high content of S at the transition between units 1 and 2 from 9.3 to 8.1 m depth in BN1 is associated with abundant tabular crystals of euhedral gypsum in the sand fraction (Fig. 2).

Unit 2 is characterized by a general decrease of salinity indicators paralleled by an increase in riverine input indicators (Figs. 2, 3). The values of elemental ratios in the upper part of unit 2 show low levels of salinity and high riverine input. In BN5, the organic-rich clayey layer at the top of unit 2 exhibits high ratios of K/Al, Rb/Al and S/Cl, while the highest concentration of S is found in the black peat horizon between ca. 7.2 and 7 m depth.

Unit 3 presents geochemical and sedimentological features characterized by high Si/Al and K/Al ratios, low salinity indices, and coarse sand and gravel most likely deposited in high-energy environment (Figs. 2, 3).

Unit 4 in BN1 shows higher than average riverine discharge and

very low levels of salinity (Fig. 2). Large peaks of K/Al and Rb/Al are associated with a 20 cm thick layer of dark brown clayey sediment at the bottom of this unit. Besides, a major peak of S/Cl at the transition between units 3 and 4 in BN1 is probably indicative of higher organic matter content. In BN5, the lower half of unit 4 between 2.9 and 1.55 m depth generally shows higher than average Rb/Al and K/Al ratios, low Si/Al ratio, and peaks of Sr/Al, whereas lower than average indicators of riverine input and salinity are most often found in the upper half of this unit above 1.55 m depth (Fig. 3).

Overall, high (low) levels of salinity in BN1 and BN5 generally correspond to low (high) levels of riverine input. Hence, the variability of salinity indicators in the ARDS could have been mainly driven by fluvial activity. Besides, the geochemical indicators of riverine discharge seem to have been influenced by the grain size of sediments. High values of Si/Al are mainly found in coarse sand and gravel (Figs. 2, 3). High values of Rb/Al are observed only in clay and silt, while high values of K/Al can be recorded in coarse or fine sediments. K and Rb are commonly associated with detrital clay (Croudace et al., 2006). However, the K/Al ratio is also influenced by the contribution of detrital K-feldspar, which may be significant in the coarse fraction (Martinez-Ruiz et al., 2015).

4.4. Magnetic susceptibility

The values of mass-specific magnetic susceptibility (χ) are generally lower than 10×10^{-8} m^{-3}·kg^{-1} in BN1 and BN5 (Figs. 2, 3). Higher than average χ values are found in the basal part of unit 1 from 12 to ca. 10 m depth in BN1 and from 18.5 to 16.9 m depth in BN5. χ values ranging between ca. 10 and 20×10^{-8} m^{-3}·kg^{-1} appear from 5.8 to 4.5 m depth in unit 2 of BN1 and from 3.3 to 2 m depth at the transition between units 3 and 4 in BN5. The highest χ values around 30×10^{-8} m^{-3}·kg^{-1} are found at the top of both cores.

Higher χ values in deltaic environment should reflect a terrigenous supply from catchment by fluvial processes (Delile et al., 2015). However, the riverine sediments of unit 3 are characterized by low χ values (Figs. 2, 3). In fact, the mineralogical composition of coarse sand and gravel can preclude the use of magnetic susceptibility as a reliable proxy record of fluvial activity. The low χ values along with high Si content and high Si/Al ratios in the sediments of unit 3 suggest that these coarse alluvial deposits are mainly composed of diamagnetic material such as quartz (Dearing, 1999; Martinez-Ruiz et al., 2015). This is confirmed by stereomicroscopic observations, which show that the alluvial deposits of unit 3 exhibit an important content of quartz for particles coarser than 1 mm.

By contrast, the high χ values of fine sediments in the upper 1.5 m of BN5 are not related to high values of elemental ratios indicative of riverine input. In fact, this increase in magnetic susceptibility could have been caused by post-depositional oxidation and weathering of sediments at the top of BN5, which is characterized by a terrestrial environment as evidenced by molluscan fauna (Figs. 3, 5).

5. Palaeoenvironmental interpretation

Delta systems in the northwestern Mediterranean are often characterized by a vertical stacking of mid-late Holocene prodelta, delta front and delta plain deposits (Dubar and Anthony, 1995; Amorosi et al., 2008, 2013c). These deltaic sequences are interpreted as highstand systems tracts deposited during the deceleration of sea level rise after 7500 cal yr BP (Stanley and Warne, 1994; Somoza et al., 1997; Vacchi et al., 2016).

The depositional environments of BN1 and BN5 can be defined on the basis of a comparison of molluscan assemblages, lithology, sediment
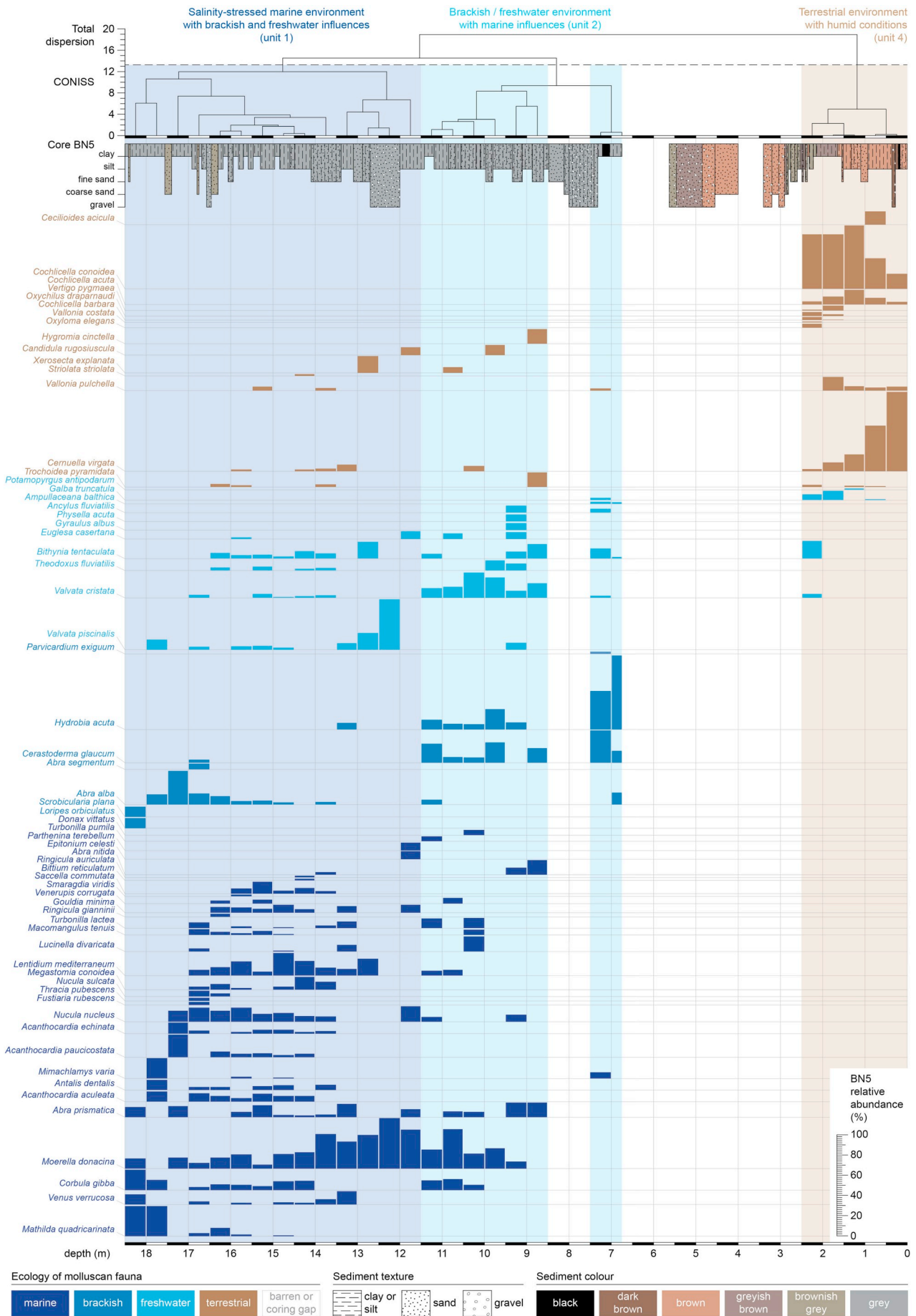
(caption on next page)

Fig. 5. Malacological diagram of core BN5. Main environmental conditions inferred from a cluster analysis by constrained incremental sum of squares (CONISS) with a dissimilarity coefficient corresponding to Edwards and Cavalli-Sforza's chord distance (Grimm, 1987).

properties and geochemical data (Figs. 2–5) with facies associations described for the northwestern Mediterranean deltas of (1) the Argens River (Allinne et al., 2006; Devillers and Bonnet, 2006; Bertoncello et al., 2014), Hérault River (Devillers et al., 2019), Rhône River (Amorosi et al., 2013c) and Var River (Dubar and Anthony, 1995) in southern France, (2) the Arno River (Amorosi et al., 2009, 2013a, 2013b), Biferno River (Amorosi et al., 2016), Po River (Amorosi et al., 2008), Posada River (Melis et al., 2018) and Tiber River (Giraudi et al., 2009) in Italy, and (3) the Ebro River (Somoza et al., 1997) and Turia River (Ruiz-Pérez and Carmona, 2019) in eastern Spain (Fig. 1A).

Holocene prodeltas in the northwestern Mediterranean are characterized by (1) salinity-stressed and strongly fluvial-influenced marine environment with abundant marine gastropods and mixed brackish-normal saline conditions, and (2) clay-sand alternations showing an upward decrease in clay content accompanied with an increase in the frequency and thickness of sandy layers (Somoza et al., 1997; Amorosi et al., 2008, 2009, 2013b, 2013c). In BN1 and BN5, unit 1 is mostly composed of grey to brownish grey clay and silty clay with intercalations of sand layers deposited in a marine environment with high levels of salinity (Figs. 2, 3). From the bottom to the top of unit 1, the sandy layers are thicker or more frequent and clay content decreases. In BN5, the presence of massive mud below 17 m depth and the increasing sand content above this depth fit well with the bottom sediment distribution of the modern inner shelf environment along the ARDS, which shows a minimum upper limit of onshore blue-grey mud and a minimum lower limit of nearshore terrigenous sand at ca. 15 m below sea level (Toutin-Morin et al., 1994). The abundance of marine molluscs ranges from ca. 45 to 75% in BN1 and from ca. 50 to 95% in BN5. Moreover, riverine inputs highlight a marine environment with fluvial influence. Hence, unit 1 is defined as a prodelta.

In the northwestern Mediterranean, the sedimentary features associated with the transition from prodelta to delta front typically exhibit an increasing proportion of sand, with a delta front composed of an upward-coarsening sand body deposited in high-energy environment (Somoza et al., 1997; Amorosi et al., 2008, 2013c). The lower and middle parts of unit 2 in BN1 and BN5 are characterized by many layers of sandy silt or fine sand, while the upper part shows upward-coarsening sand bodies in which the sand fraction changes from fine sand to medium-coarse sand from bottom to top (Figs. 2, 3). Unit 2 is also characterized by a decrease in marine shells (from ca. 50 to 0%) paralleled by a decrease in Cl/Al and an increase of riverine input (Figs. 2, 3). This unit can be considered as a ca. 5 m thick delta front, which is consistent with the delta front thickness of 5.5 and 7 m at PL1 and PAL1, respectively (Fig. 6). At BN5, the delta front is overlaid with organic-rich sediments and black peat, which were likely deposited in a marsh environment (Fig. 3).

The sediments of unit 3 are composed of poorly sorted coarse sand and clast-supported gravel devoid of fossils (Figs. 2, 3). Fining-upward trends are found in unit 3 at BN1 and from the top of unit 3 to the lower half of unit 4 at BN5. These sedimentological and biological features are typical of high-energy environments such as fluvial channels (Dubar and Anthony, 1995; Somoza et al., 1997; Amorosi et al., 2009, 2013a, 2013b, 2013c, 2016; Giraudi et al., 2009; Melis et al., 2018; Devillers et al., 2019; Ruiz-Pérez and Carmona, 2019). Moreover, a deposition of the coarse sediments of unit 3 in a river channel is consistent with the geochemical data, which show very low levels of salinity and high values of Si/Al and K/Al indicative of riverine input.

Unit 4 in BN1 and the upper half of unit 4 in BN5 are mainly composed of bioturbated brown clay, silt and fine sand with land molluscs and very low levels of salinity (Figs. 2, 3). This is compatible with a depositional environment in a well-drained floodplain occasionally affected by river floods (Somoza et al., 1997; Allinne et al.,

2006; Devillers and Bonnet, 2006; Amorosi et al., 2013a, 2016; Bertoncello et al., 2014; Melis et al., 2018; Devillers et al., 2019; Ruiz-Pérez and Carmona, 2019). The delta plain of the ARDS includes both floodplain and river channels. More specifically, the malacological data point to a delta plain environment subject to subaerial exposure, given the high abundance of terrestrial species living in coastal habitats such as *Cernuella virgata*, *Cochlicella conoidea*, *Trochoidea trochoides* and *Xerosecta explanata* at the top of BN1 and BN5 (Figs. 4, 5). Land snails and freshwater molluscs associated with humid or aquatic environment are mostly found in the lower part of unit 4 and are probably indicative of a depositional setting more frequently subjected to river flooding or hydromorphic conditions.

In BN5, the lower half of unit 4 shows thin layers of brownish grey to greyish brown sand and silt (ca. 2.9–2.2 m depth) overlaid by organic-rich greyish brown massive clay with rootlets at the top (ca. 2.2–1.5 m depth) (Fig. 3). These sediment properties and the stratigraphic relationship with the fluvial-channel deposits of unit 3 are typical of alluvial sub-environments close to river channel (Amorosi et al., 2013a, 2016). Moreover, the sediments in the lower half of unit 4 show a general fining-upward trend such as in abandoned channel fills, which are characterized by an initial proximal fill during the abandonment stage then by a distal fill collected in the abandoned palaeochannel during the disconnected stage (Toonen et al., 2012). These two stages of channel-fill development could explain the sediment deposition at ca. 2.9–2.2 and 2.2–1.5 m depth, respectively, in BN5. Besides, enhanced Sr and higher Sr/Al ratios in these sediments (Fig. 3) may indicate the presence of a shallow-water source during periods of shallowing and salinization of water bodies (Croudace et al., 2006; Martin-Puertas et al., 2011).

6. Numerical modelling

6.1. 2D age-elevation models

An accurate chronology of deltaic sequences can be difficult to determine because of ^{14}C age reversals due to sediment storage and remobilization of older deposits during downslope alluvial transport that prevails in fluvial and delta plains (Stanley and Hait, 2000; Stanley, 2001).

The median probability of 10 new radiocarbon dates obtained for BN1 and BN5 ranges from 3565 to 440 cal yr BP (Table 1). However, the 4 radiocarbon ages of charcoals and wood sampled in delta front deposits are too old and show a reversal of the median probability (Figs. 2, 3). This seems to indicate that reworking of older terrestrial organic matter from the catchment was more important in the delta front depositional environment. By excluding these 4 radiocarbon ages, the sediments from BN1 and BN5 would have been deposited approximately during the last 2500 years.

Amongst the 41 radiocarbon dates compiled in the ARDS, we discarded 12 dates (ca. 30% of total) showing age reversals with a median probability older than expected (Table 1). These reversal patterns are probably due to the remobilization and redeposition of older material (Stanley and Hait, 2000; Stanley, 2001). The cores from the ancient harbour of *Forum Iulii* (FIX, FXI, SC6) (Fig. 1B) were not used owing to potential sedimentary hiatuses caused by possible dredging in this port basin during the Roman period (Bony et al., 2011). Besides, several ^{14}C dates from the PL1 core exhibit large 2-σ uncertainty intervals higher than 300 years because of a very large plateau of the calibration curve from ca. 800 to 400 cal yr BCE (i.e. a conventional ^{14}C age around 2450 BP), the so-called Hallstatt plateau (Fontugne, 2004; Van der Plicht, 2004). Finally, a total of 29 radiocarbon ages were used to compute three 2D age-elevation models in the ARDS: one longitudinal age profile
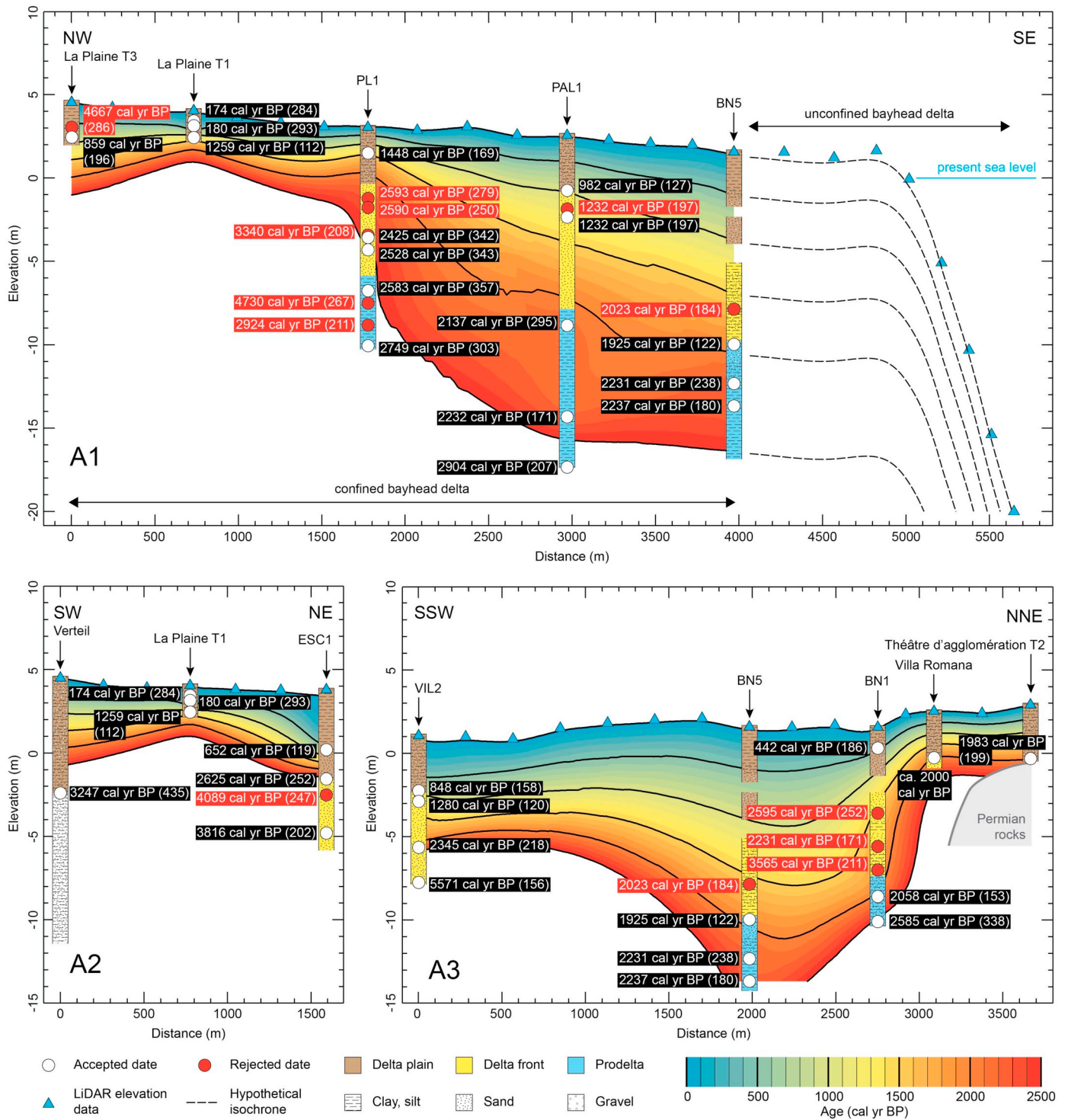
Fig. 6. 2D age-elevation models in the coastal plain of the Argens River delta system. The data used in the age-elevation models correspond to (1) the median probability of calibrated ages (white dot) from the compilation of radiocarbon ages available in the Argens River delta system (Tables 1 and 2) modern elevation based on LiDAR data (Litto3D, IGN/SHOM) for the year 2015 (blue triangle). Numbers in brackets represent the 2-σ uncertainty interval of calibrated ages (Table 1). The radiocarbon ages in red were discarded to avoid age reversals (see explanation in text). References for radiocarbon ages, lithology and depositional environment (if available): Dubar (2004) for Verteil, Allinne et al. (2006) for ESC1, Devillers and Bonnet (2006) for VIL2, Devillers et al. (2007) for Théâtre d'agglomération T2, Excoffon et al. (2010) for Villa Romana, Bertoncello et al. (2014) for PL1 and PAL1, Bertoncello et al. (2016) for La Plaine T1 and T3, and this study for BN1 and BN5. The data point for Villa Romana was estimated from the reconstruction of the shoreline around 2000 cal yr BP based on archaeological data, radiocarbon ages and relative sea level reconstruction (Excoffon et al., 2010; Vacchi et al., 2016). Location of age-elevation models A1–3 in Fig. 1B. Models interpolated with a thin plate spline kernel function and an 8-sector neighbourhood search algorithm. The isochrones of the unconfined bayhead delta were obtained by shifting the LiDAR data along the age-elevation model at BN5. (For interpretation of the references to colour in this figure legend, the reader is referred to the web version of this article.)

(A1) and two transverse age profiles (A2 and A3) across the valley (Fig. 6). The isochrones are displayed with a 100-year resolution.

Overall, profile A1 shows a downstream thickening of deposits from PL1 to BN5 over the last 2500 years. The thickest part is located between PAL1 and BN5 where a mean sediment thickness of ca. 18 m was deposited during the last 2500 years. The highest accumulation occurred between 2500 and 2000 cal yr BP in this part of profile A1. Profile A2 and the northwestern part of profile A1 exhibit a lower sediment accumulation with a thickness of ca. 5 m upstream of the ARDS during the last 2500 years. Profile A3 shows that the sediments deposited downstream of the coastal plain over the past 2500 years are thicker in the central part of the valley around BN5 and thinner on the southern edge of the ARDS, with a thickness of ca. 7 m at VIL2 (Fig. 6). On the northern side, the trench dug during the Théâtre d'agglomération T2 (TAT2) archaeological excavation revealed that Permian rocks were buried under coastal sediments during the second half of the first century BCE (Excoffon et al., 2006; Devillers et al., 2007). These Permian rocks were then covered by 2–3 m of sediments over the last 2000 years.

Although the lack of chronological data in the easternmost part of the ARDS coastal plain does not allow the age models to be robustly estimated in this area, LiDAR data were shifted along the age-elevation model at BN5 in order to propose a hypothetical reconstruction of the isochrones of the unconfined bayhead delta that prograded onto the inner shelf (Fig. 6). The depositional architecture and stacking pattern east of BN5 are thus very similar to those of steep-face deltas studied by

Dubar and Anthony (1995) along the southern French Alps, such as the Var River delta located at ca. 70 km northeast of the Argens River (Fig. 1A).

6.2. Sediment thickness

The numerical models of sediment thickness of the Argens River bayhead delta cover an area of 12.2 km^2 (Fig. 7). These spatial models were focused on the incised-valley system west of Fréjus, in which the eastward progradation of the bayhead delta of the Argens River was confined and controlled by the morphology of the valley. Moreover, the lack of data in the easternmost part of the ARDS coastal plain prevents the models to be extended east of Fréjus. Therefore, the eastern limit of the modelled area corresponds approximately to the eastern boundary of the Argens River valley between Fréjus and the eastern side of the Massif des Maures.

The thickness of sediments deposited from 2500 to 2000 cal yr BP ranges from < 1 to 8 m in the study area, with maximum values around the PAL1 site (Fig. 7A). The depocenter was located in the central part of the lower valley of the Argens River. From 2000 to 1500 cal yr BP, the depocenter moved downstream in an eastward direction (Fig. 7B). The main depositional area was located between BN5 and BN1, with a maximal thickness of deposits estimated between 4 and 5 m. Another area of moderate accumulation ranging from 1 to 3 m in thickness can be observed along a northwest-southeast direction from PL1 to PAL1.

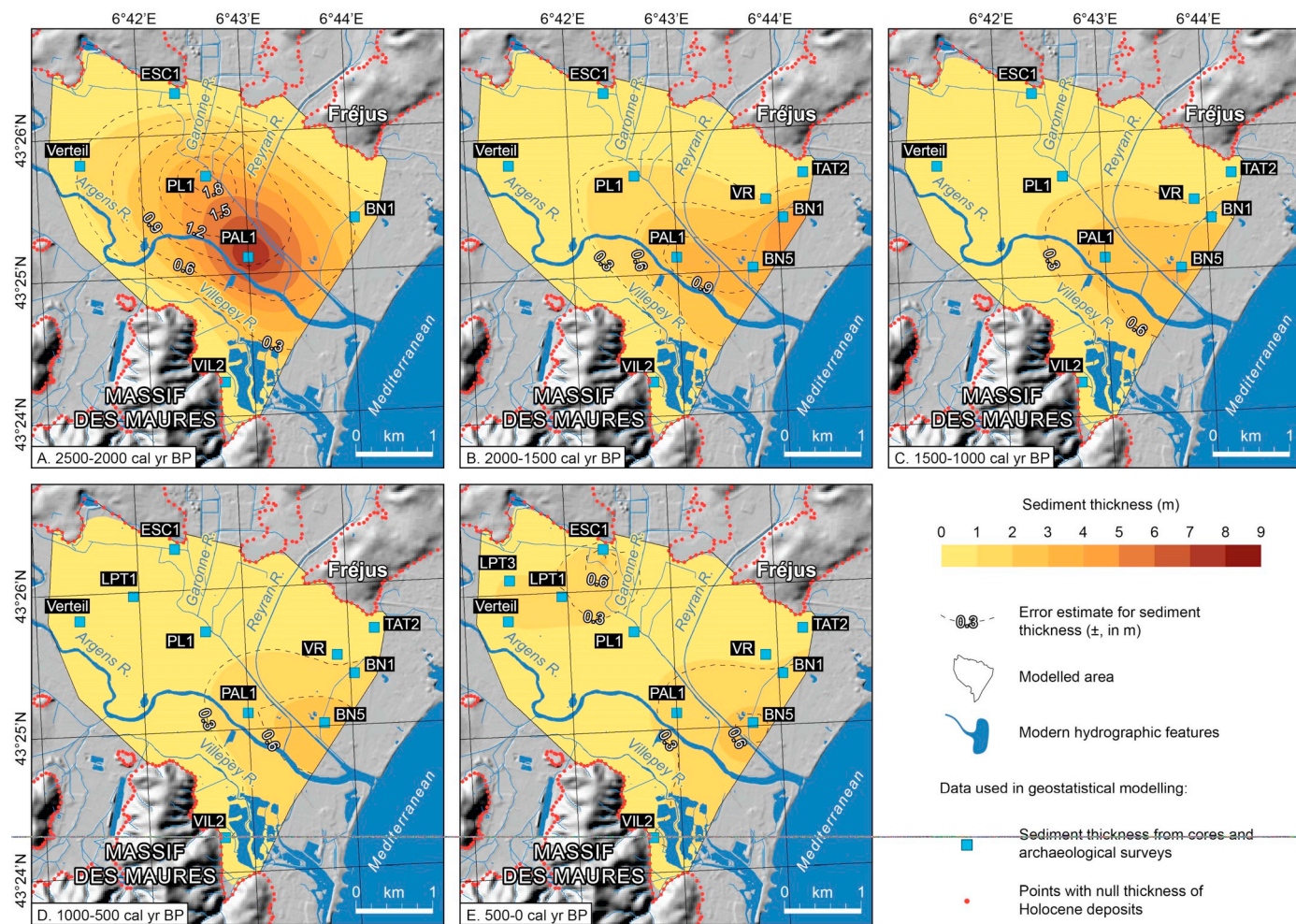After 1500 cal yr BP, the maximum accumulation of sediments was

Fig. 7. Interpolated maps of sediment thickness in the Argens River delta system over the past 2500 years. LPT1 and LPT3: La Plaine T1 and T3 archaeological surveys, TAT2: Théâtre d'agglomération T2 archaeological survey, VR: Villa Romana archaeological survey. Models interpolated with a multiquadratic kernel function and an 8-sector neighbourhood search algorithm.
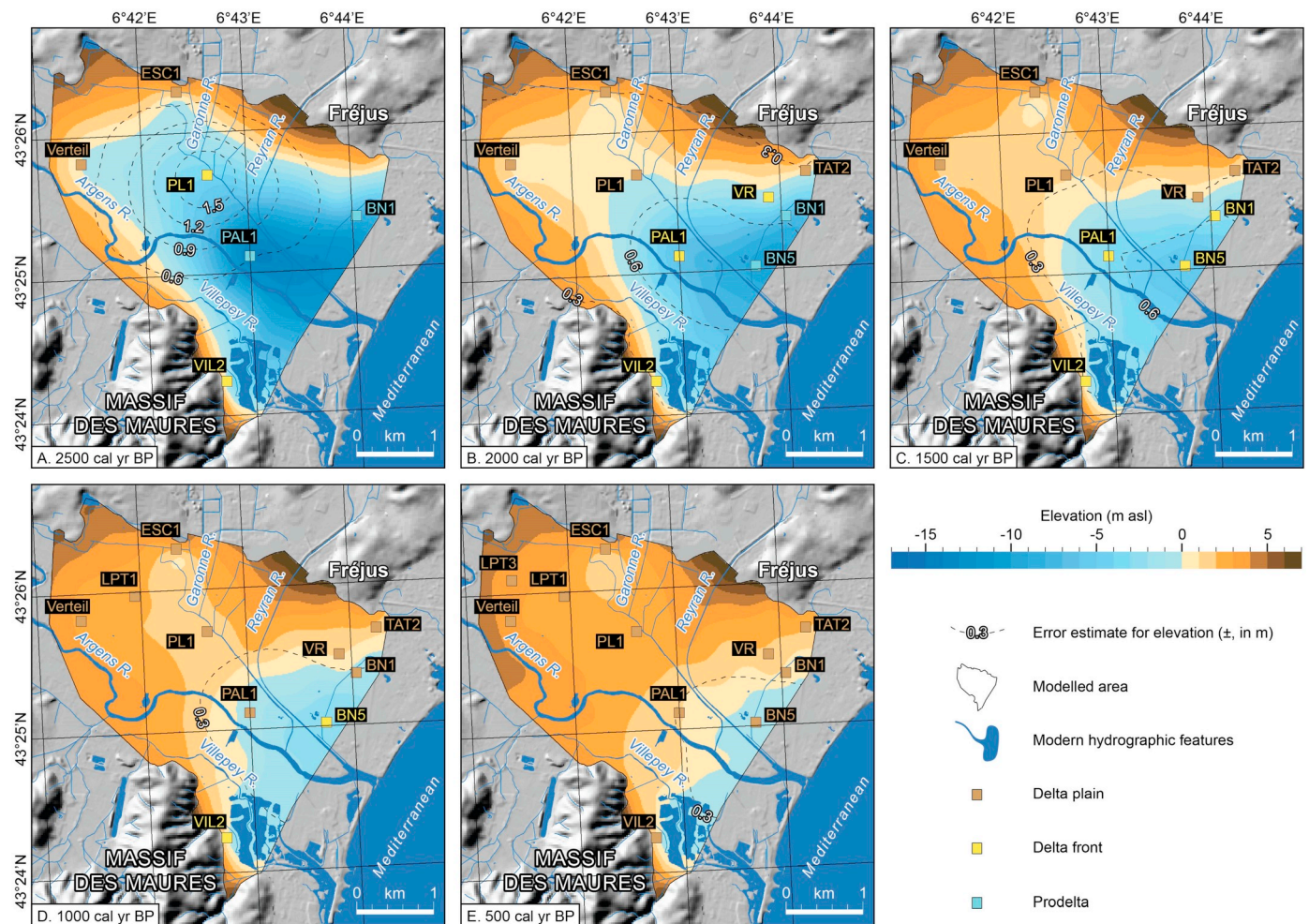
Fig. 8. Palaeoelevation in the Argens River delta system over the past 2500 years. LPT1 and LPT3: La Plaine T1 and T3 archaeological surveys, TAT2: Théâtre d'agglomération T2 archaeological survey, VR: Villa Romana archaeological survey. The past sea levels used in the elevation models are based on the relative sea level (RSL) in the western Ligurian Sea determined by the ICE-5G (VM2) geophysical model (Peltier, 2004) for the last 2500 years (Table 2). In this area, a good fit between the model and available geological sea level proxies was observed along the whole Holocene (Vacchi et al., 2016). The reconstructed RSL at 2000 cal yr BP is consistent with the Roman sea level deduced from marine encrustation found on archaeological harbour structures, a very robust methodology to infer the RSL position in the Mediterranean Sea (Morhange and Marriner, 2015; Vacchi et al., 2016). The RSL in the *Forum Iulii* harbour (Fig. 1B) was estimated at −40 ± 10 cm (Morhange et al., 2013) or −33 ± 6 cm (Devillers et al., 2007) between the first century BCE and the first century CE.

lower than 4 m for each 500-year period and the depocenter stayed close to the modern mouth of the Argens River (Fig. 7C–E). The depocenter moved southward from 1500 to 1000 cal yr BP and shows a maximum thickness of 3–4 m at BN5 (Fig. 7C). The sediment thickness pattern between 1000 and 500 cal yr BP was quite similar to the previous period, with maximum values of 2–3 m (Fig. 7D). From 500 to 0 cal yr BP, the highest sediment accumulation occurred in two areas located, on the one hand, between Verteil and ESC1, and, on the other hand, close to the mouth of the Argens River around BN5 (Fig. 7E).

6.3. Elevation modelling and coastal palaeogeography

Deltaic areas with elevation above or below sea level correspond to subaerial or subaqueous delta, respectively (Anthony, 2015). At 2500 cal yr BP, the elevation model reveals that the lower valley of the Argens River was largely occupied by a marine bay with a subaqueous delta extended until the Verteil site and a prodelta/delta front transition located between PL1 and PAL1 (Fig. 8A). The reduction in the surface area of the subaqueous delta between 2500 and 2000 cal yr BP was probably due to the progradation of the Argens, Reyran and Garonne rivers, which would have led to an eastward displacement of the prodelta/delta front transition between PAL1 and BN5 and to a decrease of

the maximum depth of the marine bay from ca. 15 to 10 m (Fig. 8A–B). Then the transition between the delta front and the prodelta moved east of BN5 after 2000 cal yr BP (Fig. 8B–C).

During the first millennium CE, elevation models suggest that land emergence seems to have been more important in the northern part of the ARDS, while subaqueous delta environment would have persisted on the southern side of the ARDS between PAL1, BN5 and VIL2 (Fig. 8B–D). The progradation in the southern part of the ARDS occurred mainly during the last millennium and would have been characterized by the formation of a fan-delta that grew between BN5 and VIL2 (Fig. 8D–E). Historical maps show that the downstream flow of the Argens River was divided into two branches at least from the end of the 16th century CE to the end of the 18th century CE (Cohen, 1997; Bertoncello et al., 2008, 2014). In addition to the southern branch of the Argens River, the Villepey River might also have contributed to the progradation in the southern part of the delta system, as shown by maps from the 18th century CE (Bertoncello et al., 2008, 2014).

At 500 cal yr BP, the elevation model suggests that a large part of the delta plain was above sea level, while a shallow body of water (< 1 m depth) oriented in a NNE-SSW direction persisted along the coastline (Fig. 8E). Moreover, a seaward progradation of ca. 1 km on average should have occurred between BN5 and VIL2 during the last

500 years, which yields a mean progradation rate of 2 m·yr^{-1}.

The present topography of the coastal plain exhibits an area of lower elevation between ESC1 and PL1 around the Garonne River, which is surrounded by two levees along the Reyran River north of PAL1 and along the Argens River between Verteil and PAL1 (Fig. 1B). The elevation models suggest that these topographic features were largely inherited over the past 2000 years (Fig. 8B–E). More specifically, the small shallow depression above sea level south of ESC1 at 500 cal yr BP (Fig. 8E) is consistent with the palaeoecological and chronological data from core ESC1, which shows the presence of a freshwater marsh from ca. 700 to 330 cal yr BP (Allinne et al., 2006).

7. Discussion

7.1. Sediment flux and fluvial activity

The elevation models were used to estimate late Holocene sediment fluxes in the ARDS (Fig. 9a). The total sediment flux in the confined bayhead delta was greatest from 2500 to 2000 cal yr BP, with a
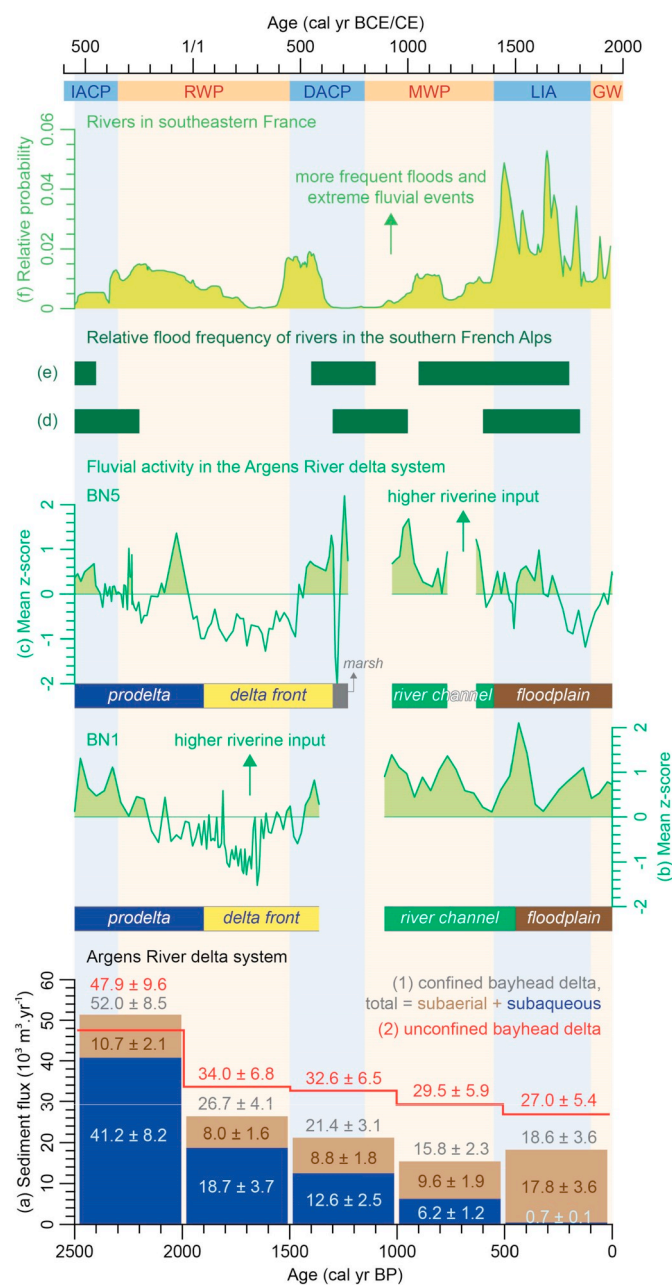

Fig. 9. Evolution of sediment flux and fluvial activity in the Argens River delta system and comparison with river flooding frequency in southeastern France over the past 2500 years. (a) Sediment fluxes calculated for each 500-year interval by estimating the volume of sediment using the ArcGIS 10 Surface Volume tool with either (1) the elevation models in Fig. 8 and reference planes corresponding to the mean relative sea level from Vacchi et al. (2016) for each 500-year interval for the confined bayhead delta, or (2) the LiDAR data shifted along the age-elevation model at BN5 (Fig. 6, age profile A1) and a reference plane at 20 m below present sea level for the unconfined bayhead delta. (b) Proxy record of riverine input and fluvial activity corresponding to the average of the standard scores of Si/Al, K/Al and Rb/Al ratios from core BN1 with an age scale established using AnalySeries 2.0 (Paillard et al., 1996), along with depositional environments. (c) Proxy record of riverine input and fluvial activity corresponding to the average of the standard scores of Si/Al, K/Al and Rb/Al ratios from core BN5 with an age scale established using AnalySeries 2.0 (Paillard et al., 1996), along with depositional environments. (d) Periods of relatively high flood frequency of the lower Durance River and its tributaries in the southern French Alps (site 1 in Fig. 1A) (Arnaud-Fassetta et al., 2010; Benito et al., 2015a). (e) Periods of relatively high flood frequency of the middle Durance River and its tributaries in the southern French Alps (site 2 in Fig. 1A) (Arnaud-Fassetta et al., 2010; Benito et al., 2015a). (f) Relative cumulative probability density function of radiocarbon dates from flood and extreme fluvial event units of rivers in southeastern France (Fig. 1A) (Benito et al., 2015a). IACP: Iron Age Cold Period, RWP: Roman Warm Period, DACP: Dark Ages Cold Period, MWP: Medieval Warm Period, LIA: Little Ice Age, GW: Global Warming.

deposition rate estimated at 52,000 ± 8500 m^3·yr^{-1}. A decrease in total sediment flux occurred after 2000 cal yr BP, with rates ranging from 15,800 ± 2300 to 26,700 ± 4100 m^3·yr^{-1}. The sediment flux in the unconfined bayhead delta along the modern delta front east of BN5 (Fig. 6) shows a general decrease from 47,900 ± 9600 to 27,000 ± 5400 m^3·yr^{-1} over the last 2500 years (Fig. 9a).

Subaerial and subaqueous sediment fluxes in the confined bayhead delta were estimated by calculating the volume of sediments above and below sea level, respectively. Subaqueous sediment flux followed a similar trend to total sediment flux. More specifically, the rates of subaqueous sediment flux declined sharply from 41,200 ± 8200 to 18,700 ± 3700 m^3·yr^{-1} between 2500 and 1500 cal yr BP, then from 6200 ± 1200 to 700 ± 100 m^3·yr^{-1} during the last millennium. Overall, subaerial sediment flux exhibits an inverse trend with rates ranging from 8000 ± 1600 to 10,700 ± 2100 m^3·yr^{-1} between 2500 and 500 cal yr BP, then increasing to 17,800 ± 3600 m^3·yr^{-1} between 500 and 0 cal yr BP (Fig. 9a). Moreover, it is worth noting that the rate of subaerial sediment flux from 2500 to 2000 cal yr BP (10,700 ± 2100 m^3·yr^{-1}) was slightly higher than that from 2000 to 1500 cal yr BP (8000 ± 1600 m^3·yr^{-1}).

Subaqueous sediment flux was ca. 2 to 4 times higher than subaerial sediment flux between 2500 and 1500 cal yr BP, while the latter exceeded the former during the last millennium. Subaerial sediment flux was 25 times higher than subaqueous sediment flux over the past 500 years. In fact, the rate of subaerial sediment flux increased sharply between 500 and 0 cal yr BP and was two times higher than during the period from 1000 to 500 cal yr BP. This sharp increase was associated with a slight increase in the total sediment flux of the confined bayhead delta between 500 and 0 cal yr BP, although this latter should be interpreted with caution given uncertainties of flux rates. Besides, the sediment flux of the unconfined bayhead delta does not seem to have significantly changed during the last millennium (Fig. 9a).

The high rates of sediment flux during the late Iron Age Cold Period (IACP) and the early Roman Warm Period (RWP) between 2500 and 2000 cal yr BP were accompanied by high levels of fluvial activity at BN1 and BN5 (Fig. 9b–c). The decrease in sediment fluxes between 2000 and 1500 cal yr BP was contemporaneous with a period of low fluvial activity in the second half of the RWP. Then the fluvial activity increased and was generally higher than average during the Dark Ages Cold Period (DACP), the Medieval Warm Period (MWP) and the Little Ice Age (LIA), except for BN5 over the last 300 years. During the late
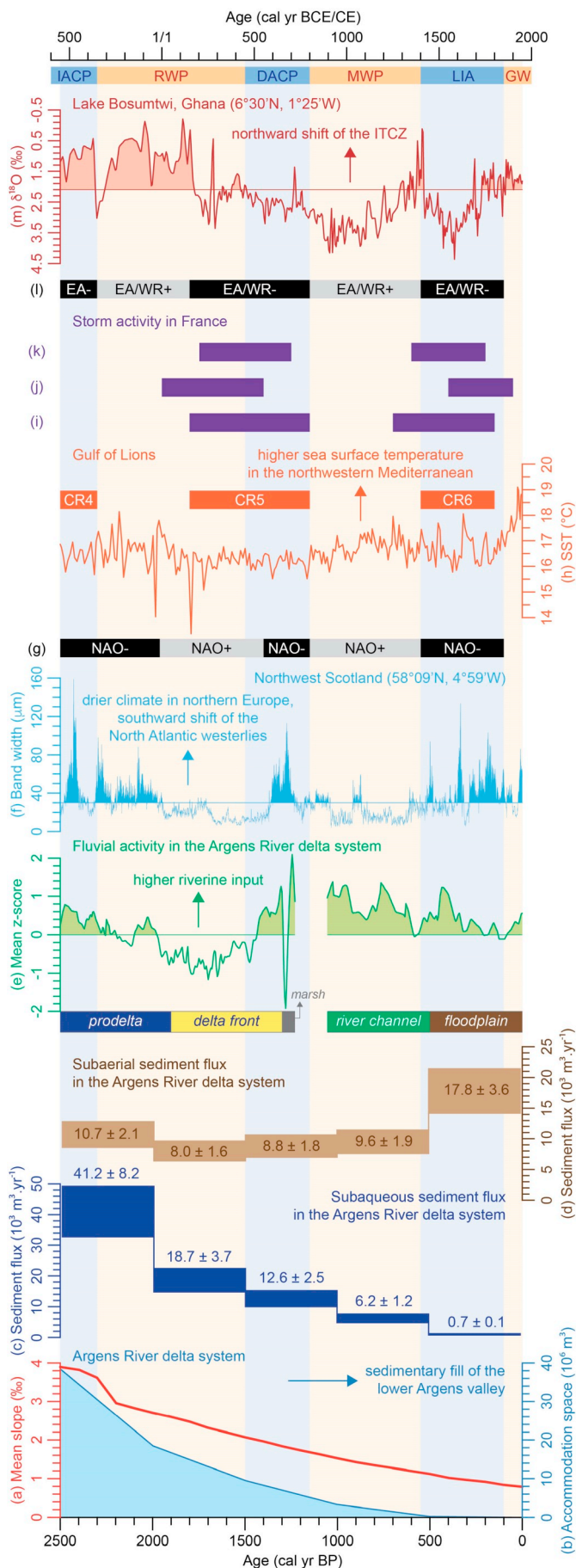
Fig. 10. Comparison of sediment flux and fluvial activity in the Argens River delta system (ARDS) with geomorphic factors and climate proxy records over the last 2500 years. (a) Longitudinal slope of the ARDS between Verteil and BN5 from age-elevation models in Fig. 6. (b) Accommodation space of the ARDS estimated using the ArcGIS 10 Surface Volume tool with the elevation models in Fig. 8 and reference planes corresponding to the relative sea level from Vacchi et al. (2016). (c) Subaqueous sediment flux in the ARDS with an error range of ± 20%. (d) Subaerial sediment flux in the ARDS with an error range of ± 20%. (e) Fluvial activity in the ARDS corresponding to the average of the standard scores of fluvial activity at BN1 and BN5 (Fig. 9b–c) resampled at a 5-year interval by linear interpolation using AnalySeries 2.0 (Paillard et al., 1996), along with depositional environments. (f) Mean band width of three radiometrically dated speleothems from the Uamh an Tartair cave in northwestern Scotland (Fig. 1A) (Proctor et al., 2002). (g) Potential leading mode of atmospheric circulation in Europe (see Section 7.3). (h) Alkenone-based sea surface temperature (SST) in the northwestern Mediterranean with cold relapse episodes (CR4–6) from core KSGC-31 in the Gulf of Lions (Fig. 1A) (Jalali et al., 2016). (i) Storm activity in southeastern France from the sedimentary record of the Bagnas lagoon (Fig. 1A) (Degeai et al., 2015). (j) Storm activity in southeastern France from the sedimentary record of the Pierre Blanche lagoon (Fig. 1A) (Sabatier et al., 2012). (k) Storm activity from sedimentary records in the Seine River estuary in northwestern France (site 4 in Fig. 11B–C) (Sorrel et al., 2009). (l) Potential second or third mode of atmospheric circulation in Europe (see Section 7.3). (m) 5-year averaged oxygen isotope record of authigenic carbonate from Lake Bosumtwi in Ghana (Fig. 1A) (Shanahan et al., 2009). NAO: North Atlantic oscillation, EA: East Atlantic pattern, EA/WR: East Atlantic/West Russian pattern, IACP: Iron Age Cold Period, RWP: Roman Warm Period, DACP: Dark Ages Cold Period, MWP: Medieval Warm Period, LIA: Little Ice Age, GW: Global Warming.

Holocene, the periods of higher than average fluvial activity in the ARDS were most often associated with increased river flooding in the southern French Alps and, more generally, with more frequent river floods and extreme fluvial events in southeastern France (Fig. 9b–f).

7.2. Autogenic control

Autogenic processes play an important role in controlling the stratigraphic architecture of bayhead delta (Simms et al., 2018). For fluvio-deltaic systems developed in incised valleys, geomorphologically-driven autogenic processes such as channel avulsion, meander cutoff, increasing levee height and tributary junction can have been controlled by changes in accommodation space and valley gradient, confluence of tributary valleys, or channel extension (Vis et al., 2010; Amorosi et al., 2013a; Simms and Rodriguez, 2015; Simms et al., 2018).

In the ARDS, the progressive decrease in longitudinal slope and accommodation space over the last 2500 years was paralleled by a general decline in subaqueous sediment flux primarily driven by geomorphic factors (Fig. 10a–c). More specifically, the lowest rate of subaqueous sediment deposition over the last 500 years could be due to limited accommodation space, which can lead to lower sediment flux during the late stages of sedimentary fill in a largely infilled estuarine basin (Clement and Fuller, 2018), i.e. in a shallow subaqueous environment.

The rate of fluvial activity associated with prodelta deposits was high during the late IACP then decreased during the first half of the RWP (Fig. 10e). This is inconsistent with the environmental evolution of western Mediterranean prodeltas that generally show an upward increase in riverine influence (Amorosi et al., 2008, 2013c). Therefore, the period of enhanced fluvial activity and high sediment flux between 2500 and 2000 cal yr BP could be indicative of an increased fluvial sedimentation caused by allogenic forcing rather than by autogenic control during delta progradation. In contrast, increasing riverine input from ca. 1700 to 1300 cal yr BP could have been autogenically controlled by delta front progradation (Fig. 10e). However, a regional increase in river flood frequency suggests that the fluvial sediment supply in the ARDS was enhanced in response to allogenic forcing (e.g. climate

change) during the DACP (Fig. 9d–f).

From ca. 1100 to 550 cal yr BP, high rates of fluvial activity and coarse sediment deposition in river channels at BN1 and BN5 were probably due to channel avulsion (Figs. 9b–c, 10e). This autogenic process was perhaps strengthened by tributary junctions of the Argens, Reyran and Villepey rivers during progradation in the easternmost part of the Argens valley (Fig. 8D–E). Nevertheless, it cannot be ruled out that high levels of fluvial activity at BN1 and BN5 during the MWP were partially controlled by allogenic forcing owing to the occurrence of episodes of more frequent river flooding in southeastern France at this time (Fig. 9b–f).

From 500 to 0 cal yr BP, although delta slope and accommodation space were very low (Fig. 10a–b), floodplain formation was associated with the highest rate of subaerial sediment flux and with higher than average levels of fluvial activity (Fig. 10d–e), in a context of high flood frequency in southeastern France (Fig. 9d–f). This suggests that fluvial sedimentation in the ARDS was closely related to allogenic factors during the LIA.

7.3. Impact of climate change

The impacts of Holocene rapid climate change on vegetation cover and hydrological regime are allogenic factors that may have controlled the fluvial and coastal sedimentation in the western Mediterranean (Fletcher and Zielhofer, 2013). The periods of higher flood frequency in this region coincided with transitions to cool and wet climatic conditions during persistent negative phases of the North Atlantic oscillation (NAO) (Wirth et al., 2013; Benito et al., 2015a).

The NAO is one of the most prominent and recurrent modes of atmospheric circulation variability in Europe (Hurrell et al., 2003). A southward (northward) shift of the North Atlantic westerly winds and storm tracks during the negative (positive) phase of the NAO leads to a wetter (drier) climate in southern Europe and to a drier (wetter) climate in northern Europe (Hurrell, 1995; Serreze et al., 1997; Osborn et al., 1999; Trigo et al., 2002). A well-known speleothem record of late Holocene climate change in northwest Scotland (Fig. 1A) was supposedly driven by the bipolar seesaw of storminess and humidity related to the NAO (Proctor et al., 2002; Trouet et al., 2009). In the ARDS, the increases in fluvial activity during the late IACP, the first half of the RWP, the DACP and the LIA were concomitant with dry periods in northern Europe and therefore should have been associated with a southward shift of the westerly winds typically found in a negative phase of the NAO (Figs. 10e–g, 11A), whereas the high rates of fluvial activity during the MWP were mainly driven by autogenic control due to delta progradation (see Section 7.2). However, increased flood frequencies in Europe may also have been influenced by other small-scale flow patterns in the atmosphere (Jacobeit et al., 2003).

Hence, we undertook an empirical orthogonal function (EOF) analysis of winter (December to February) sea level pressure (SLP) using the 500-year data set from Luterbacher et al. (2002) in order to highlight atmospheric circulation patterns in the North Atlantic and Europe (Fig. 11). The respective contributions of the three first EOFs to the total variance are estimated at 51, 20 and 14%. The leading mode EOF1 exhibits a north-south dipole with zonal flow over Europe (Fig. 11A). This NAO-like pattern is characterized by high (low) SLP anomalies over the Icelandic Low and low (high) SLP anomalies over the Azores High during its negative (positive) phase (Luterbacher et al., 2002; Josey et al., 2011), although its southern centre is offset to the east (Figs. 1A, 11A). The second mode EOF2 shows anomalously low (high) SLP over the North Sea which may be related to the negative (positive) phase of the East Atlantic/West Russian (EA/WR) pattern (Fig. 11B) (Josey et al., 2011). The third mode EOF3 is characterized by high (low) SLP anomalies centred west of the British Isles around 55°N latitude and 25°W longitude (Fig. 11C), which correspond to the negative (positive) phase of the East Atlantic (EA) pattern (Luterbacher et al., 2002; Josey et al., 2011).
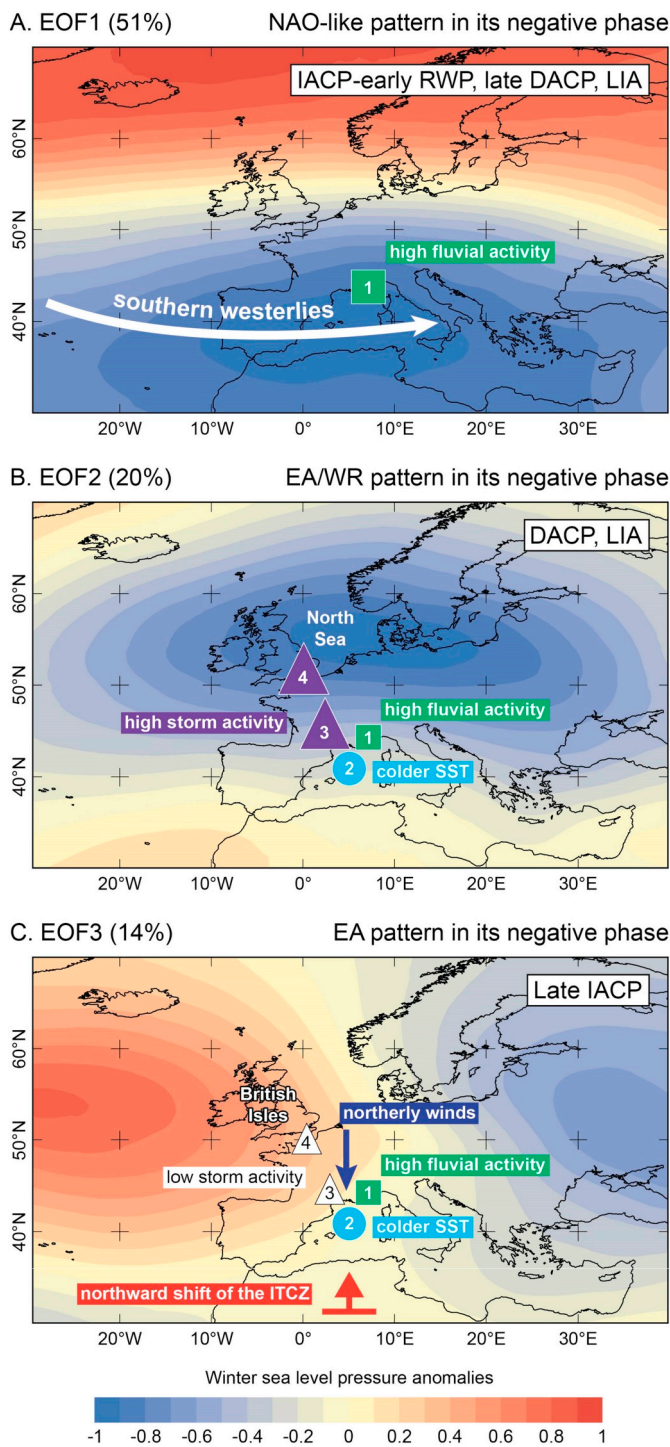

Fig. 11. Late Holocene atmospheric circulation patterns and climatic conditions in the North Atlantic and Europe during the periods of enhanced fluvial activity driven by climate change in the lower Argens valley. Empirical orthogonal functions (EOF1–3) calculated from sea level pressure reconstructed by Luterbacher et al. (2002) for the period 1500–1999 CE. 1: Fluvial activity in the Argens River delta system from this study. 2: Sea surface temperature in the northwestern Mediterranean from Jalali et al. (2016). 3: Wind storm activity in southeastern France from Degeai et al. (2015) and Sabatier et al. (2012). 4: Wind storm activity in northwestern France from Sorrel et al. (2009). SST: sea surface temperature, NAO: North Atlantic oscillation, EA: East Atlantic pattern, EA/WR: East Atlantic/West Russian pattern, ITCZ: intertropical convergence zone, IACP: Iron Age Cold Period, RWP: Roman Warm Period, DACP: Dark Ages Cold Period, LIA: Little Ice Age.

The EA/WR and EA patterns were mentioned as potential drivers of atmospheric circulation and climate change in western Europe during the late Holocene (Dermody et al., 2012; Moffa-Sanchez et al., 2014; Sanchez-Lopez et al., 2016; Sicre et al., 2016; Degeai et al., 2017). From observational data, the negative phases of the EA/WR and EA patterns were associated with higher precipitation and enhanced ocean heat loss in the northwestern Mediterranean (Qian et al., 2000; Josey et al., 2011), while strong (weak) surface winds in France were related to either a negative (positive) phase of the EA/WR pattern or a positive (negative) phase of the EA pattern (Najac et al., 2009). Hence, given the Holocene records of wind storm activity in France and of sea surface temperature (SST) in the northwestern Mediterranean (Fig. 10h–k), a negative phase of the EA pattern during the late IACP would have been followed by a positive (negative) phase of the EA/WR pattern during the lower RWP (upper RWP-DACP) and the MWP (LIA) (Fig. 10l).

In the northwestern Mediterranean, the coupling of cold northerly winds generated by winter North Atlantic blocking events during the negative phase of the EA pattern (Shabbar et al., 2001; Jiang et al., 2003; Trigo et al., 2004; Josey et al., 2011; Moffa-Sanchez et al., 2014; Sanchez-Lopez et al., 2016; Sicre et al., 2016) with warm and dry summer due to the northward position of the ITCZ (Goudeau et al., 2015) could have led to enhanced convection and higher rainfall along the southern Alps during the late IACP (Figs. 10l–m, 11C), similarly to modern heavy precipitating systems over southeastern France (Nuissier et al., 2008; Duffourg and Ducrocq, 2011). This synoptic situation could explain the high rates of sediment flux and fluvial activity in the ARDS during the late IACP (Figs. 10e, 11C).

The positive phase of the EA/WR pattern during the lower RWP from ca. 2300 to 1800 cal yr BP was associated with a large-scale circulation pattern characterized by a negative or positive phase of the NAO (Fig. 10g, l). This period shows a decreasing trend in fluvial activity in the ARDS apart from the 2nd and 1st centuries BCE (Fig. 10e). During the lower RWP, the ITCZ was still in a northern position (Fig. 10m), but the absence or low frequency of atmospheric blocking events and cold northerly winds would have limited atmospheric convection and precipitation in the southern Alps. From 1800 to 1150 cal yr BP, i.e. during the late RWP and the DACP, a general increase in fluvial activity in the ARDS would have occurred during a negative phase of the EA/WR pattern, with higher than average rates when both EA/WR and NAO patterns were in a negative phase between 1400 and 1150 cal yr BP (Fig. 10e, g, l).

In the Western Mediterranean, there is a broad consensus on the climatic conditions of the MWP (LIA), which were generally warm (cold) and dry (wet) from continental records in Spain (Martin-Puertas et al., 2008, 2010; Martin-Chivelet et al., 2011; Moreno et al., 2012; Sanchez-Lopez et al., 2016), Italy (Frisia et al., 2005; Mensing et al., 2016; Sadori et al., 2016), southern France (Degeai et al., 2017) and northern Morocco (Wassenburg et al., 2013). A positive (negative) phase of the NAO pattern would have been combined with a positive (negative) phase of the EA/WR pattern during the MWP (LIA) (Fig. 10g, l). Besides, the climatic context of the LIA would have been similar to that of the DACP (Fig. 11B).

The sharp increase in subaerial sediment flux in the ARDS between 500 and 0 cal yr BP (Fig. 10d) is consistent with the hydrogeomorphic response to environmental change in the western Mediterranean during the LIA, which was characterized by more frequent flooding and enhanced fluvial activity (Barriendos Vallve and Martin-Vide, 1998; Wilhelm et al., 2012; Wirth et al., 2013; Benito et al., 2015a; Degeai et al., 2017) along with an increase in detrital inputs of terrigenous material in marine sediments at sites KSGC-31 (Jalali et al., 2016), MD99-2343 (Frigola et al., 2007), 305G–306G (Nieto-Moreno et al., 2011), 384B–436B (Nieto-Moreno et al., 2013a, 2013b) and DP30 (Goudeau et al., 2014, 2015) (Fig. 1A). Overall, high fluvial sediment supply and rapid delta growth in an increasingly human-influenced environment occurred along the Mediterranean coasts after 500 cal yr BP (Anthony et al., 2014). However, it is currently difficult to assess the real contribution of human land use to late Holocene sediment flux in the ARDS because of the lack of quantitative data to measure the magnitude of the geomorphic impact of anthropogenic forcing.

8. Conclusion

The palaeogeographic reconstruction of a deltaic system is challenging because the geomorphic evolution in coastal areas is often influenced by rapid changes in relative sea level, shoreline progradation, sedimentation rate and climatic conditions. A new multi-method approach using cores and archaeological trenches, geochemistry and magnetic susceptibility of sediments, malacology, radiocarbon chronology, geostatistics and numerical modelling was undertaken in order to robustly characterize changes in environmental conditions, geomorphic setting and sediment flux associated with delta growth in incised-valley systems. This quantitative method was applied to the bayhead delta of the Argens River in the western Mediterranean, in order to assess the impacts of autogenic control and climate change on the variations in sediment flux and fluvial activity of this deltaic system.

The coastal dynamics of the Argens River delta were studied over the last 2500 years. Four major facies associations were identified from the bottom to the top of the deltaic depositional system: (1) a prodelta with clay-sand alternations deposited in a marine environment with brackish or freshwater influences and high levels of salinity, (2) a delta front characterized by higher sand content as well as by coarsening-upward trend and gradual increase in riverine input, (3) river channels filled with sand and gravel, and (4) a floodplain with a high abundance of land snails and with low salinity levels.

Late Holocene sediment fluxes were estimated from numerical modelling then compared with hydroclimate proxy records and geomorphic factors. An overall decrease in subaqueous sediment supply over the last 2500 years could have been geomorphologically controlled by autogenic processes such as changes in accommodation space and delta slope. High rates of sediment flux between 2500 and 2000 cal yr BP coincided with episodes of increased river flooding in southeastern France. The maximum rate of subaerial sediment flux from 500 to 0 cal yr BP could have been caused by high fluvial activity and more frequent flood events during the cold and wet climatic conditions of the Little Ice Age.

In general, high sediment fluxes at 2500–2000 and 500–0 cal yr BP were associated with higher than average levels of fluvial activity in the Argens River delta system. Climate-driven increases in fluvial activity in this deltaic system over the past 2500 years seem to be associated with a southward shift of the North Atlantic westerlies and storm tracks in southern Europe. This atmospheric circulation pattern could have been combined with either (1) a negative phase of the East Atlantic pattern coupled to a northward migration of the intertropical convergence zone during the late Iron Age Cold Period, or (2) a negative phase of the East Atlantic/West Russian pattern during the Dark Ages Cold Period and the Little Ice Age.

This quantitative approach will need to be applied to other Mediterranean deltas in order to compare the variation of coastal sediment fluxes in response to hydroclimate change and geomorphic setting over the past millennia. Besides, the study of other deltaic sequences will be needed to firmly establish a link between delta sedimentation and atmospheric circulation patterns in the western Mediterranean. Furthermore, the analysis of palaeobotanical, archaeological and historical data will be required to accurately estimate the impact of human land use on sediment flux and geomorphic change in these coastal areas.

C2FN (DT INSU, CNRS, EQUIPEX CLIMCOR, Investissements d'Avenir ANR-11-EQPX-0009) and the BRGM. The sedimentological analyses were done at the ArcheoEnvironnement Laboratory (CNRS UMR5140). We thank Dr. Edward Anthony (editor) and two anonymous reviewers for their helpful remarks and suggestions that improved the manuscript.

Data availability

http://dx.doi.org/10.17632/p5fbtmwnsr.1.

References

Allinne, C., Devillers, B., Bertoncello, F., Bouby, L., Bruneton, H., Bui Thi, M., Cade, C., Revil, A., 2006. Archéologie et paléoenvironnement sur le site du pont romain des Esclapes (Fréjus, Var). ArcheoSciences 30, 181–196.

Amorosi, A., Milli, S., 2001. Late Quaternary depositional architecture of Po and Tevere river deltas (Italy) and worldwide comparison with coeval deltaic successions. Sediment. Geol. 144, 357–375.

Amorosi, A., Centineo, M.C., Colalongo, M.L., Fiorini, F., 2005. Millennial-scale depositional cycles from the Holocene of the Po Plain, Italy. *Mar. Geol.* 222-223, 7–18.

Amorosi, A., Dinelli, E., Rossi, V., Vaiani, S.C., Sacchetto, M., 2008. Late Quaternary palaeoenvironmental evolution of the Adriatic coastal plain and the onset of Po River Delta. Palaeogeogr. Palaeoclimatol. Palaeoecol. 268, 80–90.

Amorosi, A., Lucchi, M.R., Rossi, V., Sarti, G., 2009. Climate change signature of small-scale parasequences from Lateglacial–Holocene transgressive deposits of the Arno valley fill. Palaeogeogr. Palaeoclimatol. Palaeoecol. 273, 142–152.

Amorosi, A., Bini, M., Giacomelli, S., Pappalardo, M., Ribecai, C., Rossi, V., Sammartino, I., Sarti, G., 2013a. Middle to late Holocene environmental evolution of the Pisa coastal plain (Tuscany, Italy) and early human settlements. Quat. Int. 303, 93–106.

Amorosi, A., Rossi, V., Sarti, G., Mattei, R., 2013b. Coalescent valley fills from the late Quaternary record of Tuscany (Italy). Quat. Int. 288, 129–138.

Amorosi, A., Rossi, V., Vella, C., 2013c. Stepwise post-glacial transgression in the Rhône Delta area as revealed by high-resolution core data. Palaeogeogr. Palaeoclimatol. Palaeoecol. 374, 314–326.

Amorosi, A., Bracone, V., Campo, B., D'Amico, C., Rossi, V., Rosskopf, C.M., 2016. A late Quaternary multiple paleovalley system from the Adriatic coastal plain (Biferno River, Southern Italy). Geomorphology 254, 146–159.

Anthony, E.J., 2015. Wave influence in the construction, shaping and destruction of river deltas: a review. Mar. Geol. 361, 53–78.

Anthony, E.J., Marriner, N., Morhange, C., 2014. Human influence and the changing geomorphology of Mediterranean deltas and coasts over the last 6000 years: from progradation to destruction phase? Earth Sci. Rev. 139, 336–361.

Arnaud-Fassetta, G., Carcaud, N., Castanet, C., Salvador, P.-G., 2010. Fluviatile palaeoenvironments in archaeological context: geographical position, methodological approach – hydrological risk issues. Quat. Int. 216, 93–117.

Barriendos Vallve, M., Martin-Vide, J., 1998. Secular climatic oscillations as indicated by catastrophic floods in the Spanish Mediterranean coastal area (14th–19th centuries). Clim. Chang. 38, 473–491.

Benito, G., Macklin, M.G., Zielhofer, C., Jones, A.F., Machado, M.J., 2015a. Holocene flooding and climate change in the Mediterranean. Catena 130, 13–33.

Benito, G., Macklin, M.G., Panin, A., Rossato, S., Fontana, A., Jones, A.F., Machado, M.J., Matlakhova, E., Mozzi, P., Zielhofer, C., 2015b. Recurring flood distribution patterns related to short-term Holocene climatic variability. Sci. Rep. 5 (16398), 1–8.

Bertoncello, F., Bonnet, S., Bouby, L., Delhon, C., Devillers, B., Guillon, S., 2008. Projet Collectif de Recherches «Occupation du sol et patrimoine archéologique dans la basse vallée de l'Argens». Rapport de fin de projet. Rapport pour le Ministère de la Culture et de la Communication, CEPAM, Nice (124 p).

Bertoncello, F., Bonnet, S., Excoffon, P., Bony, G., Morhange, C., Gébara, C., Georges, K., Devillers, B., 2011. Dynamique du littoral et peuplement: le cas de la colonie romaine de Fréjus. In: Pasqualini, M. (Ed.), Fréjus romaine, la ville et son territoire. Agglomérations de Narbonnaise, des Alpes-Maritimes et de Cisalpine à travers la recherche archéologique. Editions APDCA, Antibes, pp. 75–87.

Bertoncello, F., Devillers, B., Bonnet, S., Guillon, S., Bouby, L., Delhon, C., 2014. Mobilité des paysages littoraux et peuplement dans la basse vallée de l'Argens (Var, France) au cours de l'Holocène. Quaternaire 25 (1), 23–44.

Bertoncello, F., Bernigaud, N., Burri, S., Degeai, J.-P., Delhon, C., Digelmann, P., Gayet, F., Jansen, P., Mercuri, L., Ouriachi, M.-J., Porra, M., Portalier, N., Purdue, L., Romagnan, B., Segura, J.-A., Vaschalde, C., 2016. Projet Collectif de Recherches, Dynamiques du peuplement et des paysages dans le territoire de Fréjus. Rapport final 2014–2016. Rapport pour le Ministère de la Culture et de la Communication, CEPAM, Nice (115 p).

Bony, G., Morhange, C., Bruneton, H., Carbonel, P., Gébara, C., 2011. 2000 ans de colmatage du port antique de Fréjus (*Forum Julii*), France: une double métamorphose littorale. Compt. Rendus Geosci. 343, 701–715.

Chagué-Goff, C., Dawson, S., Goff, J.R., Zachariasen, J., Berryman, K.R., Garnett, D.L., Waldron, H.M., Mildenhall, D.C., 2002. A tsunami (ca. 6300 years BP) and other Holocene environmental changes, northern Hawke's Bay, New Zealand. Sediment. Geol. 150, 89–102.

Clement, A.J.H., Fuller, I.C., 2018. Influence of system controls on the Late Quaternary geomorphic evolution of a rapidly-infilled incised-valley system: the lower Manawatu valley, North Island New Zealand. Geomorphology 303, 13–29.

Cohen, O., 1997. La baie de Fréjus: 2000 ans d'évolution du rivage. Mappemonde 1, 6–12.

Croudace, I.W., Rindby, A., Rothwell, R.G., 2006. ITRAX: description and evaluation of a new multi-function X-ray core scanner. In: Rothwell, R.G. (Ed.), New Techniques in Sediment Core Analysis. Geological Society, London, Special Publications 267. pp. 51–63.

Dalrymple, R.W., Zaitlin, B.A., Boyd, R., 1992. Estuarine facies models: conceptual basis and stratigraphic implications. J. Sediment. Petrol. 62 (6), 1130–1146.

Dearing, J., 1999. Environmental Magnetic Susceptibility Using the Bartington MS2 System. Bartington Instruments, Oxford (43 p).

Degeai, J.-P., Devillers, B., Dezileau, L., Oueslati, H., Bony, G., 2015. Major storm periods and climate forcing in the Western Mediterranean during the Late Holocene. Quat. Sci. Rev. 129, 37–56.

Degeai, J.-P., Devillers, B., Blanchemanche, P., Dezileau, L., Oueslati, H., Tillier, M., Bohbot, H., 2017. Fluvial response to the last Holocene rapid climate change in the Northwestern Mediterranean coastlands. Glob. Planet. Chang. 152, 176–186.

Delile, H., Abichou, A., Gadhoum, A., Goiran, J.-P., Pleuger, E., Monchambert, J.-Y., Wilson, A., Fentress, E., Quinn, J., Ben Jerbania, I., Ghozzi, F., 2015. The geoarchaeology of Utica, Tunisia: the paleogeography of the Mejerda Delta and hypotheses concerning the location of the ancient harbour. Geoarchaeology 30, 291–306.

Dermody, B.J., De Boer, H.J., Bierkens, M.F.P., Weber, S.L., Wassen, M.J., Dekker, S.C., 2012. A seesaw in Mediterranean precipitation during the Roman Period linked to millennial-scale changes in the North Atlantic. Clim. Past 8, 637–651.

Devillers, B., Bonnet, S., 2006. 6000 ans d'histoire environnementale de la lagune de Villepey (Fréjus, Var): premiers résultats de l'étude multi-proxies de la carotte Vil2. ArcheoSciences 30, 197–203.

Devillers, B., Excoffon, P., Morhange, C., Bonnet, S., Bertoncello, F., 2007. Relative sea-level changes and coastal evolution at *Forum Julii* (Fréjus, Provence). Compt. Rendus Geosci. 339, 329–336.

Devillers, B., Bony, G., Degeai, J.-P., Gasco, J., Lachenal, T., Bruneton, H., Yung, F., Oueslati, H., Thierry, A., 2019. Holocene coastal environmental changes and human occupation of the lower Hérault River, southern France. Quat. Sci. Rev. 222, 105912.

Dezileau, L., Sabatier, P., Blanchemanche, P., Joly, B., Swingedouw, D., Cassou, C., Castaings, J., Martinez, P., Von Grafenstein, U., 2011. Intense storm activity during the Little Ice Age on the French Mediterranean coast. Palaeogeogr. Palaeoclimatol. Palaeoecol. 299, 289–297.

Dezileau, L., Pérez-Ruzafa, A., Blanchemanche, P., Degeai, J.-P., Raji, O., Martinez, P., Marcos, C., Von Grafenstein, U., 2016. Extreme storms during the last 6500 years from lagoonal sedimentary archives in the Mar Menor (SE Spain). Clim. Past 12, 1389–1400.

Dubar, M., 2004. L'édification de la plaine deltaïque du Bas Argens (Var, France) durant la Protohistoire et l'Antiquité. Application d'un modèle numérique 2D à l'archéologie. Méditerranée 102, 47–54.

Dubar, M., Anthony, E.J., 1995. Holocene environmental change and river-mouth sedimentation in the Baie des Anges, French Riviera. Quat. Res. 43, 329–343.

Dubar, M., Bui-Thi, M., Nicol-Pichard, S., Thinon, M., 2004. Étude palynologique du carottage de Pont d'Argens (Roquebrune-sur-Argens, Var): histoire holocène de la végétation en Provence cristalline; facteurs naturels et anthropiques. Ecologia Mediterranea 30 (2), 147–157.

Duffourg, F., Ducrocq, V., 2011. Origin of the moisture feeding the Heavy Precipitating Systems over Southeastern France. Nat. Hazards Earth Syst. Sci. 11, 1163–1178.

Durozoy, G., Gouvernet, C., Jonquet, P., Theillier, P., 1970. Inventaire des ressources hydrauliques dans la basse vallée de l'Argens (Var). BRGM, Orléans (39 p).

EPA, 2007. Method 6200: Field Portable X-ray Fluorescence Spectrometry for the Determination of Elemental Concentrations in Soil and Sediment. United Stated Environmental Protection Agency (32 p.). https://www.epa.gov/sites/production/files/2015-12/documents/6200.pdf.

Excoffon, P., Devillers, B., Bonnet, S., Bouby, L., 2006. Nouvelles données sur la position du littoral antique de Fréjus. Le diagnostic archéologique du "théâtre d'agglomération" (Fréjus, Var). ArcheoSciences 30, 205–221.

Excoffon, P., Bonnet, S., Devillers, B., Berger, J.-F., 2010. L'évolution de trait de côte aux abords de Fréjus, de sa foundation jusqu'à la fin du Ier siècle après J.-C. In: Delestre, X., Marchesi, H. (Eds.), Archéologie des rivages méditerranéens: 50 ans de recherche. Actes du colloque d'Arles (Bouches-du-Rhône) 28-29-30 octobre 2009 Errance, Paris, pp. 47–53.

Fletcher, W.J., Zielhofer, C., 2013. Fragility of Western Mediterranean landscapes during Holocene rapid climate changes. Catena 103, 16–29.

Fletcher, W.J., Debret, M., Sanchez-Goni, M.F., 2013. Mid-Holocene emergence of a low-frequency millennial oscillation in western Mediterranean climate: implications for past dynamics of the North Atlantic atmospheric westerlies. The Holocene 23 (2), 153–166.

Fontugne, M., 2004. Les derniers progrès du calibrage des âges radiocarbone permettent-ils une révision des chronologies entre 25 et 50.000 ans B.P.? Quaternaire 15 (3), 245–252.

Frigola, J., Moreno, A., Cacho, I., Canals, M., Sierro, F.J., Flores, J.A., Grimalt, J.O., Hodell, D.A., Curtis, J.H., 2007. Holocene climate variability in the western Mediterranean region from a deepwater sediment record. Paleoceanography 22, PA2209.

Frisia, S., Borsato, A., Spötl, C., Villa, I.M., Cucchi, F., 2005. Climate variability in the SE Alps of Italy over the past 17 000 years reconstructed from a stalagmite record. Boreas 34, 445–455.

Gascou, J., 1982. Quand la colonie de Fréjus fut-elle fondée? Latomus 41 (1), 132–145.

Gascou, J., Janon, M., 1985. Inscriptions Latines de Narbonnaise (I.L.N.)- Fréjus. Gallia (Suppl. 44) (229 p).

Gébara, C., Morhange, C., 2010. Fréjus (*Forum Julii*): le port antique/the ancient harbour. *J. Roman Archaeol.*(Suppl. 77) (152 p).

Giaime, M., Marriner, N., Morhange, C., 2019. Evolution of ancient harbours in deltaic contexts: a geoarchaeological typology. Earth Sci. Rev. 191, 141–167.

Giraudi, C., Tata, C., Paroli, L., 2009. Late Holocene evolution of Tiber River Delta and geoarchaeology of Claudius and Trajan Harbor, Rome. Geoarchaeology 24 (3), 371–382.

Goudeau, M.-L.S., Grauel, A.-L., Tessarolo, C., Leider, A., Chen, L., Bernasconi, S.M., Versteegh, G.J.M., Zonneveld, K.A.F., Boer, W., Alonso-Hernandez, C.M., De Lange, G.J., 2014. The Glacial–Interglacial transition and Holocene environmental changes in sediments from the Gulf of Taranto, central Mediterranean. Mar. Geol. 348, 88–102.

Goudeau, M.-L.S., Reichart, G.-J., Wit, J.C., De Nooijer, L.J., Grauel, A.-L., Bernasconi, S.M., De Lange, G.J., 2015. Seasonality variations in the Central Mediterranean during climate change events in the Late Holocene. Palaeogeogr. Palaeoclimatol. Palaeoecol. 418, 304–318.

Grimm, E.C., 1987. Coniss: a Fortran 77 program for stratigraphically constrained cluster analysis by the method of incremental sum of squares. Comput. Geosci. 13 (1), 13–35.

Grove, A.T., 2001. The "Little Ice Age" and its geomorphological consequences in Mediterranean Europe. Clim. Chang. 48, 121–136.

Haenssler, E., Nadeau, M.-J., Vött, A., Unkel, I., 2013. Natural and human induced environmental changes preserved in a Holocene sediment sequence from the Etoliko Lagoon, Greece: new evidence from geochemical proxies. Quat. Int. 308-309, 89–104.

Hurrell, J.W., 1995. Decadal trends in the North Atlantic Oscillation: regional temperatures and precipitation. Science 269, 676–679.

Hurrell, J.W., Kushnir, Y., Ottersen, G., Visbeck, M., 2003. An overview of the North Atlantic Oscillation. In: Hurrell, J.W., Kushnir, Y., Ottersen, G., Visbeck, M. (Eds.), The North Atlantic Oscillation: Climatic Significance and Environmental Impact. Geophysical Monograph 134. American Geophysical Union, Washington D.C., pp. 1–35.

Jacobeit, J., Glaser, R., Luterbacher, J., Wanner, H., 2003. Links between flood events in central Europe since AD 1500 and large-scale atmospheric circulation modes. Geophys. Res. Lett. 30 (4), 1172.

Jalali, B., Sicre, M.-A., Bassetti, M.-A., Kallel, N., 2016. Holocene climate variability in the North-Western Mediterranean Sea (Gulf of Lions). Clim. Past 12, 91–101.

Jiang, Q., Smith, R.B., Doyle, J., 2003. The nature of the mistral: observations and modelling of two MAP events. Q. J. R. Meteorol. Soc. 129, 857–875.

Josey, S.A., Somot, S., Tsimplis, M., 2011. Impacts of atmospheric modes of variability on Mediterranean Sea surface heat exchange. J. Geophys. Res.-Oceans 116, C02032.

Koster, K., Stafleu, J., Cohen, K.M., 2017. Generic 3D interpolation of Holocene base-level rise and provision of accommodation space, developed for the Netherlands coastal plain and infilled palaeovalleys. Basin Res. 29, 775–797.

Lambeck, K., Bard, E., 2000. Sea-level change along the French Mediterranean coast for the past 30 000 years. Earth Planet. Sci. Lett. 175, 203–222.

Lopez-Buendia, A.M., Bastida, J., Querol, X., Whateley, M.K.G., 1999. Geochemical data as indicators of palaeosalinity in coastal organic-rich sediments. Chem. Geol. 157, 235–254.

Luterbacher, J., Xoplaki, E., Dietrich, D., Rickli, R., Jacobeit, J., Beck, C., Gyalistras, D., Schmutz, C., Wanner, H., 2002. Reconstruction of sea level pressure fields over the Eastern North Atlantic and Europe back to 1500. Clim. Dyn. 18, 545–561.

Makclin, M.G., Benito, G., Gregory, K.J., Johnstone, E., Lewin, J., Michczynska, D.J., Soja, R., Starkel, L., Thorndycraft, V.R., 2006. Past hydrological events reflected in the Holocene fluvial record of Europe. Catena 66, 145–154.

Martin-Chivelet, J., Munoz-Garcia, M.B., Edwards, R.L., Turrero, M.J., Ortega, A.I., 2011. Land surface temperature changes in Northern Iberia since 4000 yr BP, based on δ13C of speleothems. Glob. Planet. Chang. 77, 1–12.

Martinez-Ruiz, F., Kastner, M., Gallego-Torres, D., Rodrigo-Gamiz, M., Nieto-Moreno, V., Ortega-Huertas, M., 2015. Paleoclimate and paleoceanography over the past 20,000 yr in the Mediterranean Sea Basins as indicated by sediment elemental proxies. Quat. Sci. Rev. 107, 25–46.

Martin-Puertas, C., Valero-Garcés, B.L., Mata, M.P., Gonzalez-Sampériz, P., Bao, R., Moreno, A., Stefanova, V., 2008. Arid and humid phases in southern Spain during the last 4000 years: the Zonar Lake record, Cordoba. Holocene 18 (6), 907–921.

Martin-Puertas, C., Jiménez-Espejo, F., Martinez-Ruiz, F., Nieto-Moreno, V., Rodrigo, M., Mata, M.P., Valero-Garcés, B.L., 2010. Late Holocene climate variability in the southwestern Mediterranean region: an integrated marine and terrestrial geochemical approach. Clim. Past 6, 807–816.

Martin-Puertas, C., Valero-Garcés, B.L., Mata, M.P., Moreno, A., Giralt, S., Martinez-Ruiz, F., Jiménez-Espejo, F., 2011. Geochemical processes in a Mediterranean Lake: a high-resolution study of the last 4,000 years in Zonar Lake, southern Spain. J. Paleolimnol. 46, 405–421.

Melis, R.T., Di Rita, F., French, C., Marriner, N., Montis, F., Serreli, G., Sulas, F., Vacchi, M., 2018. 8000 years of coastal changes on a western Mediterranean island: a multiproxy approach from the Posada plain of Sardinia. Mar. Geol. 403, 93–108.

Mensing, S., Tunno, I., Cifani, G., Passigli, S., Noble, P., Archer, C., Piovesan, G., 2016. Human and climatically induced environmental change in the Mediterranean during the Medieval Climate Anomaly and Little Ice Age: a case from central Italy. Anthropocene 15, 49–59.

Milli, S., D'Ambrogi, C., Bellotti, P., Calderoni, G., Carboni, M.G., Celant, A., Di Bella, L., Di Rita, F., Frezza, V., Magri, D., Pichezzi, R.M., Ricci, V., 2013. The transition from wave-dominated estuary to wave-dominated delta: the Late Quaternary stratigraphic architecture of Tiber River deltaic succession (Italy). Sediment. Geol. 284–285, 159–180.

Moffa-Sanchez, P., Born, A., Hall, I.R., Thornalley, D.J.R., Barker, S., 2014. Solar forcing of North Atlantic surface temperature and salinity over the past millennium. Nat. Geosci. 7, 275–278.

Moreno, A., Pérez, A., Frigola, J., Nieto-Moreno, V., Rodrigo-Gámiz, M., Martrat, B., González-Sampériz, P., Morellón, M., Martín-Puertas, C., Corella, J.P., Belmonte, A., Sancho, C., Cacho, I., Herrera, G., Canals, M., Grimalt, J.O., Jiménez-Espejo, F.,

Martínez-Ruiz, F., Vegas-Vilarrúbia, T., Valero-Garcés, B.L., 2012. The Medieval Climate Anomaly in the Iberian Peninsula reconstructed from marine and lake records. Quat. Sci. Rev. 43, 16–32.

Morhange, C., Marriner, N., 2015. Archeological and biological relative sea-level indicators. In: Shennan, I., Long, A.J., Horton, B.P. (Eds.), Handbook of Sea-level Research. Wiley Works Series AGU, Wiley, pp. 146–156.

Morhange, C., Marriner, N., Excoffon, P., Bonnet, S., Flaux, C., Zibrowius, H., Goiran, J.-P., El Amouri, M., 2013. Relative sea-level changes during Roman times in the Northwest Mediterranean: the 1st century A.D. fish tank of *Forum Julii*, Fréjus, France. Geoarchaeology 28 (4), 363–372.

Najac, J., Boé, J., Terray, L., 2009. A multi-model ensemble approach for assessment of climate change impact on surface winds in France. Clim. Dyn. 32, 615–634.

Nieto-Moreno, V., Martinez-Ruiz, F., Giralt, S., Jiménez-Espejo, F., Gallego-Torres, D., Rodrigo-Gamiz, M., Garcia-Orellana, J., Ortega-Huertas, M., de Lange, G.J., 2011. Tracking climate variability in the western Mediterranean during the Late Holocene: a multiproxy approach. Clim. Past 7, 1395–1414.

Nieto-Moreno, V., Martinez-Ruiz, F., Giralt, S., Gallego-Torres, D., Garcia-Orellana, J., Masqué, P., Ortega-Huertas, M., 2013a. Climate imprints during the 'Medieval Climate Anomaly' and the 'Little Ice Age' in marine records from the Alboran Sea basin. The Holocene 23 (9), 1227–1237.

Nieto-Moreno, V., Martinez-Ruiz, F., Willmott, V., Garcia-Orellana, J., Masqué, P., Sinninghe Damsté, J.S., 2013b. Climate conditions in the westernmost Mediterranean over the last two millennia: an integrated biomarker approach. Org. Geochem. 55, 1–10.

Nuissier, O., Ducrocq, V., Ricard, D., Lebeaupin, C., Anquetin, S., 2008. A numerical study of three catastrophic precipitating events over southern France. I: numerical framework and synoptic ingredients. Q. J. R. Meteorol. Soc. 134, 111–130.

Osborn, T.J., Briffa, K.R., Tett, S.F.B., Jones, P.D., Trigo, R.M., 1999. Evaluation of the North Atlantic Oscillation as simulated by a coupled climate model. Clim. Dyn. 15, 586–702.

Paillard, D., Labeyrie, L., Yiou, P., 1996. Macintosh program performs time-series analysis. EOS Transactions AGU 77 (39), 379.

Peltier, W.R., 2004. Global glacial isostasy and the surface of the ice-age Earth: the ICE-5G (VM2) model and GRACE. Annu. Rev. Earth Planet. Sci. 32, 111–149.

Proctor, C.J., Baker, A., Barnes, W.L., 2002. A three thousand year record of North Atlantic climate. Clim. Dyn. 19, 449–454.

Qian, B., Corte-Real, J., Xu, H., 2000. Is the North Atlantic Oscillation the most important atmospheric pattern for precipitation in Europe? J. Geophys. Res. 105, 11,901–11,910.

Reimer, P.J., Bard, E., Bayliss, A., Beck, J.W., Blackwell, P.G., Ramsey, C.B., Buck, C.E., Cheng, H., Edwards, R.L., Friedrich, M., Grootes, P.M., Guilderson, T.P., Haflidason, H., Hajdas, I., Hatté, C., Heaton, T.J., Hoffmann, D.L., Hogg, A.G., Hughen, K.A., Kaiser, K.F., Kromer, B., Manning, S.W., Niu, M., Reimer, R.W., Richards, D.A., Scott, E.M., Southon, J.R., Staff, R.A., Turney, C.S.M., Van der Plicht, J., 2013. Intcal13 and Marine13 radiocarbon age calibration curves 0–50,000 years cal BP. Radiocarbon 55 (4), 1869–1887.

Rodrigo-Gamiz, M., Martinez-Ruiz, F., Jiménez-Espejo, F.J., Gallego-Torres, D., Nieto-Moreno, V., Romero, O., Ariztegui, D., 2011. Impact of climate variability in the western Mediterranean during the last 20,000 years: oceanic and atmospheric responses. Quat. Sci. Rev. 30, 2018–2034.

Rodrigo-Gamiz, M., Martinez-Ruiz, F., Rodriguez-Tovar, F.J., Jimenez-Espejo, F.J., Pardo-Iguzquiza, E., 2014. Millennial- to centennial-scale climate periodicities and forcing mechanisms in the westernmost Mediterranean for the past 20,000 yr. Quat. Res. 81, 78–93.

Ruiz-Pérez, J.-M., Carmona, P., 2019. Turia river delta and coastal barrier-lagoon of Valencia (Mediterranean coast of Spain): geomorphological processes and global climate fluctuations since Iberian-Roman times. Quat. Sci. Rev. 219, 84–101.

Sabatier, P., Dezileau, L., Condomines, M., Briqueu, L., Colin, C., Bouchette, F., Le Duff, M., Blanchemanche, P., 2008. Reconstruction of paleostorm events in a coastal lagoon (Hérault, South of France). Mar. Geol. 251, 224–232.

Sabatier, P., Dezileau, L., Colin, C., Briqueu, L., Bouchette, F., Martinez, P., Siani, G., Raynal, O., Von Grafenstein, U., 2012. 7000 years of paleostorm activity in the NW Mediterranean Sea in response to Holocene climate events. Quat. Res. 2012, 1–11.

Sadori, L., Giraudi, C., Masi, A., Magny, M., Ortu, E., Zanchetta, G., Izdebski, A., 2016. Climate, environment and society in southern Italy during the last 2000 years. A review of the environmental, historical and archaeological evidence. Quat. Sci. Rev. 136, 173–188.

Sanchez-Lopez, G., Hernandez, A., Pla-Rabes, S., Trigo, R.M., Toro, M., Granados, I., Saez, A., Masqué, P., Pueyo, J.J., Rubio-Inglés, M.J., Giralt, S., 2016. Climate reconstruction for the last two millennia in central Iberia: the role of East Atlantic (EA), North Atlantic Oscillation (NAO) and their interplay over the Iberian Peninsula. Quat. Sci. Rev. 149, 135–150.

Schofield, J.E., Edwards, K.J., Mighall, T.M., Martinez Cortizas, A., Rodriguez-Racedo, J., Cook, G., 2010. An integrated geochemical and palynological study of human impacts, soil erosion and storminess from southern Greenland since c. AD 1000. Palaeogeogr. Palaeoclimatol. Palaeoecol. 295, 19–30.

Serreze, M.C., Carse, F., Barry, R.G., Rogers, J.C., 1997. Icelandic low cyclone activity: climatological features, linkages with the NAO, and relationships with recent changes in the Northern Hemisphere circulation. J. Clim. 10, 453–464.

Shabbar, A., Huang, J., Higuchi, K., 2001. The relationship between the wintertime North Atlantic oscillation and blocking episodes in the North Atlantic. Int. J. Climatol. 21, 355–369.

Shanahan, T.M., Overpeck, J.T., Anchukaitis, K.J., Beck, J.W., Cole, J.E., Dettman, D.L., Peck, J.A., Scholz, C.A., King, J.W., 2009. Atlantic forcing of persistent drought in West Africa. Science 324, 377–380.

Siani, G., Paterne, M., Arnold, M., Bard, E., Métivier, B., Tisnerat, N., Bassinot, F., 2000.

Radiocarbon reservoir ages in the Mediterranean Sea and Black Sea. Radiocarbon 42 (2), 271–280.

Sicre, M.-A., Jalali, B., Martrat, B., Schmidt, S., Bassetti, M.-A., Kallel, N., 2016. Sea surface temperature variability in the North Western Mediterranean Sea (Gulf of Lion) during the Common Era. Earth Planet. Sci. Lett. 456, 124–133.

Simms, A.R., Rodriguez, A.B., 2015. The influence of valley morphology on the rate of bayhead delta progradation. J. Sediment. Res. 85, 38–44.

Simms, A.R., Rodriguez, A.B., Anderson, J.B., 2018. Bayhead deltas and shorelines: insights from modern and ancient examples. Sediment. Geol. 374, 17–35.

Somoza, L., Barnolas, A., Arasa, A., Maestro, A., Rees, J.G., Hernandez-Molina, F.J., 1997. Architectural stacking patterns of the Ebro delta controlled by Holocene high-frequency eustatic fluctuations, delta-lobe switching and subsidence processes. Sediment. Geol. 117, 11–32.

Sorrel, P., Tessier, B., Demory, F., Delsinne, N., Mouazé, D., 2009. Evidence for millennial-scale climatic events in the sedimentary infilling of a macrotidal estuarine system, the Seine estuary (NW France). Quat. Sci. Rev. 28, 499–516.

Spada, G., Stocchi, P., 2007. SELEN: a Fortran 90 program for solving the "sea-level equation". Comput. Geosci. 33, 538–562.

Stanley, J.-D., 2001. Dating modern deltas: progress, problems, and prognostics. Annu. Rev. Earth Planet. Sci. 29, 257–294.

Stanley, J.-D., Hait, A.K., 2000. Deltas, radiocarbon dating, and measurements of sediment storage and subsidence. Geology 28 (4), 295–298.

Stanley, J.-D., Warne, A.G., 1994. Worldwide initiation of Holocene marine deltas by deceleration of sea-level rise. Science 265 (5169), 228–231.

Striewski, B., Mayr, C., Flenley, J., Naumann, R., Turner, G., Lücke, A., 2009. Multi-proxy evidence of late Holocene human-induced environmental changes at Lake Pupuke, Auckland (New Zealand). Quat. Int. 202, 69–93.

Stuiver, M., Reimer, P.J., Reimer, R.W., 2019. CALIB 7.1. [WWW program] at. http://calib.org.

Toonen, W.H.J., Kleinhans, M.G., Cohen, K.M., 2012. Sedimentary architecture of abandoned channel fills. Earth Surf. Process. Landf. 37, 459–472.

Toutin-Morin, N., Bonijoly, D., Brocard, C., Broutin, J., Crévola, G., Dardeau, G., Dubar, M., Féraud, J., Giraud, J.D., Godefroy, P., Laville, P., Meinesz, A., 1994. Notice explicative, Carte géologique de la France (1/50000), feuille Fréjus-Cannes (1024). BRGM Editions, Orléans (187 p).

Trigo, I.F., Bigg, G.R., Davies, T.D., 2002. Climatology of cyclogenesis mechanisms in the Mediterranean. Mon. Weather Rev. 130, 549–569.

Trigo, R.M., Trigo, I.F., DaCamara, C.C., Osborn, T.J., 2004. Climate impact of the European winter blocking episodes from the NCEP/NCAR Reanalyses. Clim. Dyn. 23, 17–28.

Trouet, V., Esper, J., Graham, N.E., Baker, A., Scourse, J.D., Frank, D.C., 2009. Persistent positive North Atlantic Oscillation mode dominated the Medieval Climate Anomaly. Science 324, 78–80.

Trouet, V., Scourse, J.D., Raible, C.C., 2012. North Atlantic storminess and Atlantic Meridional Overturning Circulation during the last Millennium: reconciling contradictory proxy records of NAO variability. Glob. Planet. Chang. 84-85, 48–55.

Vacchi, M., Marriner, N., Morhange, C., Spada, G., Fontana, A., Rovere, A., 2016. Multiproxy assessment of Holocene relative sea-level changes in the western Mediterranean: sea-level variability and improvements in the definition of the isostatic signal. Earth Sci. Rev. 155, 172–197.

Van der Plicht, J., 2004. Radiocarbon, the calibration curve and Scythian chronology. In: Scott, E.M., Alekseev, A.Y., Zaitseva, G. (Eds.), Impact of the Environment on Human Migration in Eurasia. NATO Science Series, IV Earth and Environmental Sciences 42. Springer, Netherlands, pp. 45–61.

Véron, A., Morhange, C., Poirier, A., Angeletti, B., Bertoncello, F., 2018. Geochemical markers of human occupation in the lower Argens valley (Fréjus, France): from protohistory to Roman times. J. Archaeol. Sci. Rep. 17, 242–249.

Vis, G.-J., Bohncke, S.J.P., Schneider, H., Kasse, C., Coenraads-Nederveen, S., Zuurbier, K., Rozema, J., 2010. Holocene flooding history of the Lower Tagus Valley (Portugal). J. Quat. Sci. 25 (8), 1222–1238.

Wassenburg, J.A., Immenhauser, A., Richter, D.K., Niedermayr, A., Riechelmann, S., Fietzke, J., Scholz, D., Jochum, K.P., Fohlmeister, J., Schröder-Ritzrau, A., Sabaoui, A., Riechelmann, D.F.C., Schneider, L., Esper, J., 2013. Moroccan speleothem and tree ring records suggest a variable positive state of the North Atlantic Oscillation during the Medieval Warm Period. Earth Planet. Sci. Lett. 375, 291–302.

Wilhelm, B., Arnaud, F., Sabatier, P., Crouzet, C., Brisset, E., Chaumillon, E., Disnar, J.-R., Guiter, F., Malet, E., Reyss, J.-L., Tachikawa, K., Bard, E., Delannoy, J.-J., 2012. 1400 years of extreme precipitation patterns over the Mediterranean French Alps and possible forcing mechanisms. Quat. Res. 78, 1–12.

Wirth, S.B., Glur, L., Gilli, A., Anselmetti, F.S., 2013. Holocene flood frequency across the Central Alps – solar forcing and evidence for variations in North Atlantic atmospheric circulation. Quat. Sci. Rev. 80, 112–128.